DEVELOPMENT OF THERMAL TESTING TECHNIQUES AT HIGH SOLAR INTENSITIES

Final Report

June 1967

CONTRACT NAS 2-3164

Prepared for

AMES RESEARCH CENTER

NATIONAL AERONAUTICS AND SPACE ADMINISTRATION

Aerospace Sciences Laboratory

Lockheed Palo Alto Research Laboratory

LOCKHEED MISSILES & SPACE COMPANY

A Group Division of Lockheed Aircraft Corporation

Palo Alto, California

NOTICE

This report was prepared as an account of Government sponsored work. Neither the United States, nor the National Aeronautics and Space Administration (NASA), nor any person acting on behalf of NASA:

A. Makes any warranty or representation, expressed or implied, with respect to the accuracy, completeness, or usefulness of the information contained in this report, or that the use of any information, apparatus, method, or process disclosed in this report may not infringe privately owned rights; or

B. Assumes any liabilities with respect to the use of, or for damages resulting from the use of any information, apparatus, method or process disclosed in this report.

As used above, "person acting on behalf of NASA" includes any employee or contractor of NASA, or employee of such contractor, to the extent that such employee or contractor of NASA, or employee of such contractor prepares, disseminates, or provides access to, any information pursuant to his employment or contract with NASA, or his employment with such contractor.

DEVELOPMENT OF
THERMAL TESTING TECHNIQUES
AT HIGH SOLAR INTENSITIES

by R. E. Rolling and K. N. Marshall

June 1967

FOREWORD

This report was prepared by the Lockheed Palo Alto Research Laboratory of Lockheed Missiles & Space Company, for the Ames Research Center of the National Aeronautics and Space Administration. The work was performed under Contract NAS 2-3164 and was administered by the Systems Engineering Division of Ames Research Center, with Mr. J.P. Kirkpatrick as project monitor.

The work described in this report was performed from 13 August 1965 to 13 May 1967. This is the final report for this contract.

ACKNOWLEDGMENTS

ILLUSTRATIONS

CONTENTS

TABLES

Section 1

SUMMARY

Thermal performance testing of spacecraft which must function at distances near to the solar disk will require the availability of extremely high energy flux levels. Presently available solar simulators are limited in maximum intensity to approximately 2 suns. For spacecraft approaching to within 0.2 AU of the solar disk, it will be necessary to simulate with approximately 25 solar constants.

Several energy simulation techniques were investigated in terms of their potential use in performance testing of vehicles which function at near-solar distances. These included carbon arc, xenon arc, filtered xenon arc, and tungsten filament lamps. Both analytical and experimental results were obtained on a half-scale model of an advanced Pioneer-type spacecraft to establish the sensitivity of the prototype thermal design to the various kinds of simulation. The model design utilized an external thermal control surface similar to that proposed for the hardware and was tested using a carbon arc solar simulator at 1 solar constant and using tungsten lamp simulation at 1, 5, and 9 solar constants. A thermal analyzer program, based upon the model design, was used to predict test temperatures of the model and to forecast its actual space performance.

The results obtained from the study indicated that testing of the spacecraft with high quality carbon arc or filtered xenon-arc simulators would result in a satisfactory indication of flight performance, although actual flight temperature would not be duplicated. Similar testing with high-temperature tungsten filament lamps will require filtering of all energy emitted at wavelengths beyond 4.5 μ due to the spectrally selective surfaces used on the exterior of the vehicle.

Section 2

INTRODUCTION

The present series of Pioneer spacecraft is conducting a systematic exploration of the environment in interplanetary space between 0.8 and 1.2 AU (ref. 1). As part of this program, an advanced Pioneer has been conceived which will extend the coverage to within 0.2 AU. This spacecraft will experience intense solar irradiation (25 solar constants) at this distance. To satisfactorily perform throughout the entire mission requires extensive use of the most advanced thermal control techniques available. In view of the complexities involved in the thermal design, it is obvious that thermal performance verification for the final hardware is a most important part of the overall program. Provision of solar simulation for the performance evaluation was the major consideration of the work described in this report.

The spacecraft design must be relatively insensitive to the solar environment in order to survive the intense irradiation as it approaches the sun. At the same time, the interior portions must be maintained at reasonable temperatures at near-earth distances. Both requirements are met by utilizing a minimum number of appendages (booms, antennas, etc.), isolating the interior with high performance insulation, providing active thermal control for the equipment platform, and by placing a movable heat shield in front of the solar arrays. This design not only satisfies the thermal control requirements but also results in a spacecraft that is relatively insensitive to the imperfections in collimation and energy distribution of a solar simulator. However, the distribution of thermal control surfaces and solar cells proposed for the exterior of the satellite makes it quite sensitive to spectral mismatch between the simulator and the extraterrestrial sun.

There is little doubt that the spacecraft could be performance tested with a high degree of accuracy using a well collimated solar simulator with a close match to the solar spectrum. Unfortunately, no such facility presently exists with the capability of providing from 0.14 to 3.5 W/cm^2 over a 2-m-diameter test plane. This leads to consideration of other possible techniques such as the use of high-temperature tungsten lamps for absorbed heat-flux simulation. Such approaches have been described in detail by several investigators (refs. 2,3,4) and appear to hold promise for the present application where extreme flux levels are required. However, implementation of the technique must be considered in terms of the differing spectrally selective surfaces used on major exterior portions of the spacecraft.

The objective of the work described in this report was to study the difficulties involved in using tungsten simulation for performance testing of the final hardware. The work was completed in two separate phases and was both analytical and experimental in nature. The program as initially conceived involved an analytical study of the space thermal performance of the spacecraft based upon an early conception of spacecraft design. The analysis was also used to predict the thermal performance of the spacecraft under space-simulated conditions using a variety of sources. This work has been completed and will be referred to in the remainder of this report as Phase I of the overall study effort. The results of the analysis were previously reported in ref. 5.

2

The results obtained from the initial analytical study indicated that internal components would be maintained at acceptable levels throughout the flight. It was also found that simulation sources such as the carbon arc or filtered xenon arc would provide test results of a realistic nature for thermal performance testing. In addition, the results suggested that the spacecraft thermal design may require some modification. It was found that overheating of solar cell arrays was a strong possibility unless some form of active thermal control was provided to shield the arrays at perihelion. The density of solar cells on the upper array required modification since the temperatures of that array with full solar cell coverage were predicted to be in excess of 590°K. Design changes were made to overcome these potential difficulties and a new conceptual configuration was established for further study.

The results obtained from the prototype thermal analyses were of significant value in delineating problem areas that existed both in thermal design and testing of the hardware. It was also found, through parametric studies, that significantly different predictions of thermal performance would be obtained for variations in thermal properties within the range of expected uncertainties. In view of the changes made in spacecraft design and the uncertainties in specifying actual thermal properties, a decision was made to design, fabricate, and test a half-scale thermal model of the conceptual solar-powered spacecraft. The analytical and experimental program conducted on the model is the primary subject of this report.

The objective of the Phase II effort was to construct a small-scale thermal model of the modified spacecraft and to subject this model to test procedures similar to those proposed for use in testing of the prototype hardware. All major nodes of the thermal analyzer network used in Phase I were duplicated in the model although exact conformance with the model laws was not possible in all cases. Following construction and testing of the model, the thermal analyzer program was modified to conform with the model design so that predictions of model performance could be made. In this manner the computer program was utilized to verify performance of the model in the space chamber and to compare this performance with that predicted for actual flight conditions.

The Phase II study disclosed that considerable error may be caused by the direct use of high-temperature tungsten filament lamp simulation. The major source of difficulty is infrared emission from the quartz enclosure. Energy from this source is absorbed in large quantity by the special thermal control surfaces used on the spacecraft and will result in overheating at all flux levels. Procedures must be implemented to eliminate this energy from the incident flux. The results also disclosed that the thermal analyzer program used to predict performance does not give an adequate correlation between experiment and analysis. The difficulty was attributed to the effects of the many penetrations and edges of the multilayer insulation used in construction of the model. These influences on thermal performance of the insulation must be better understood to construct a more accurate thermal analyzer model of the prototype spacecraft.

Section 3
NOMENCLATURE

A	area
A_p	projected area
AU	astronomical unit
F	radiation geometric view factor
K	thermal conductivity
kW	kilowatts
L	length dimension
Q	internal rate of energy dissipation
S	incident external energy flux density
T	absolute temperature
V	volts
W	watts
α	absorptance
α_s	solar absorptance
ϵ	total hemispherical emittance
μ	microns

Section 4

SPACECRAFT CONFIGURATION

Several possible spacecraft configurations have been considered for near-solar missions. A solar-powered design and a radioisotope thermoelectric generator (RTG) design were selected for study during the present research program. The solar-powered concept uses solar cells to provide the electrical power required for vehicle equipment operation, while the RTG concept employs two RTG units for power generation. Both configurations require rather sophisticated thermal design, with extensive use of the optical solar reflector (OSR) thermal control surface and high performance multilayer insulation, in order to survive the severe thermal environment of a 1.0- to 0.2-AU solar mission. During the Phase I portion of the program, the thermal performance of both configurations was considered in detail. The space thermal performance of each was predicted analytically and reported in ref. 5. A summary description of the Phase I thermal analysis is presented in Appendix A of this report.

During Phase II, the investigation was limited to further study of the solar-powered concept. A sketch of this design is shown in Figure 1. Major sections of the spacecraft are: (1) antenna reflector and dipole; (2) upper solar array; (3) experiment viewing band; (4) lower solar cell array; (5) lower array heat shield; (6) experiment booms; (7) internal equipment platform; and (8) louver system for active thermal control. The main body of the spacecraft is 91.5 cm in diameter and approximately 91.5 cm high. The antenna reflector and dipole extend approximately 132 cm above the top of the vehicle; the experiment booms are 152 cm in length.

The skin of the upper and lower solar cell arrays is composed of 0.635 cm (1/4 in.) thick aluminum honeycomb with 0.0254 cm (0.010 in.) thick fiberglass facing sheets on each side. The external surface of the upper solar array is covered with a mosaic of filtered silicon solar cells and OSR in a combination selected to keep the array temperature at acceptable levels throughout the mission. The surface of the lower array is covered entirely with solar cells that are protected by the variable aperture heat shield that is programmed to allow a maximum solar cell temperature of 366° K. The viewing band is entirely covered with OSR and has 12 penetrations of various sizes and shapes that provide experiment apertures and sun sensor and boom mountings. All apertures are covered with a layer of aluminized polyimide film, except two apertures which are open. The experiment booms are entirely coated with OSR.

The spacecraft is spinning at a rate of 60 rpm; however, both the antenna reflector and lower array heat shield are despun. The external surface of the heat shield is coated with OSR, and the inner surface facing the lower array is aluminized

DIMENSIONS IN
CENTIMETERS

(1) Antenna Reflector and Dipole
(2) Upper Solar Cell Array
(3) Experiment Viewing Band
(4) Lower Solar Cell Array
(5) Lower Array Heat Shield
(6) Experiment Booms
(7) Internal Equipment Platform
(8) Louver System for Active Thermal Control
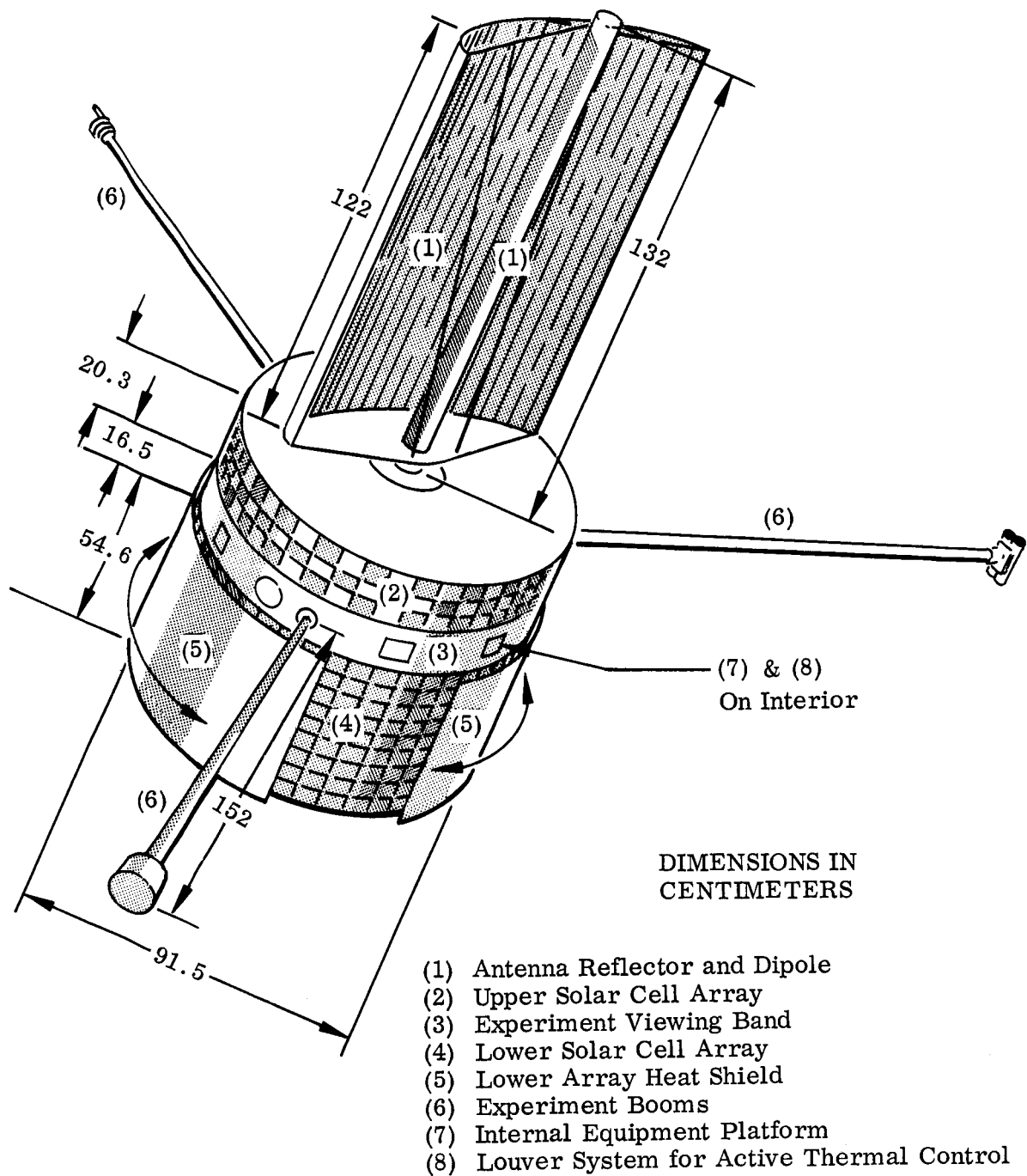
Figure 1 Spacecraft Solar-Powered Configuration

to provide a low emittance. The antenna reflector has OSR on the convex surface and white thermal control paint on the concave surface.

The equipment platform is the central supporting member for all major structural components and is composed of aluminum honeycomb with aluminum facing sheets. The equipment compartment is thermally isolated from the exterior by high-performance multilayer insulation attached to the skin inner surfaces and by insulating spacers located between structural attachment points. Energy entering the internal region through the insulation, through protuberances, and through openings in addition to 50 W of internal power is radiated to space by the active louver system located directly below the equipment platform. Certain critical components mounted on the platform require that temperature be maintained at near-earth ambient levels (approximately 272° to 305°K) throughout the entire mission.

The extreme external thermal environment of the anticipated mission is illustrated in Figure 2, which shows the variation of incident solar heat flux on a flat plate in going from 1 to 0.2 AU. The OSR surfaces protecting the vehicle from this thermal environment are highly stable and have an α_s/ϵ of approximately 0.06 (ref. 6). The OSR is basically a second surface mirror composed of vacuum-deposited silver on fused silica (ref. 7). Spectral reflectance characteristics between 0.28 and 22 μ are provided in Figure 3 for this surface, for the filtered silicon solar cell, and for a typical white thermal control paint.

The multilayer insulation blankets used to isolate the internal regions are composed of alternate layers of aluminized polyimide film and a fiberglass spacer material. For this application the nominal effective thermal conductivity of the blankets is estimated to be on the order of 8.6 × 10^{-6} W/cm °K (5 × 10^{-4} Btu/hr ft °R) for all sections of the vehicle except the viewing band where the penetrations and blanket size will cause a reduction in this value (refs. 8—9). For this region the effectiveness of the blanket may be reduced to the order of 8.6 × 10^{-5} W/cm °K (5 × 10^{-3} Btu/hr ft °R), although experimental confirmation of this estimate is unavailable.

The thermal analyzer computer model established during the Phase I portion of the program was used to predict the behavior of the spacecraft for 1 and 25 suns of extraterrestrial solar irradiation. Following these computations, the boundary conditions were changed to conform to the thermal inputs expected for simulation testing with carbon arc, xenon, and filtered xenon simulating sources. These computations were based on spectral data similar to those shown in Figure 4 and were made at only 1 solar constant since present sources are limited to near this condition for the required 2-m-diameter test plane. Results of these computations are given in Table 1 for vehicle regions of primary interest. Comparison of the results obtained indicated that any of these simulators would provide satisfactory simulation for performance testing of the spacecraft. The largest variation occurred in the lower solar cell array using xenon simulation where a 10°K temperature difference was observed, as compared with the predicted solar performance at 1 solar constant. The largest variations for the other sources were 4°K for the filtered xenon and 1°K for the carbon arc on the lower array. These differences in temperature are due to changes in total
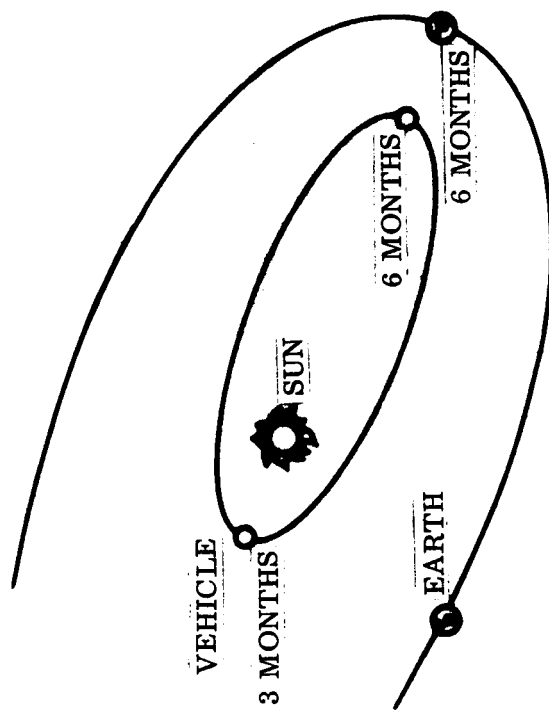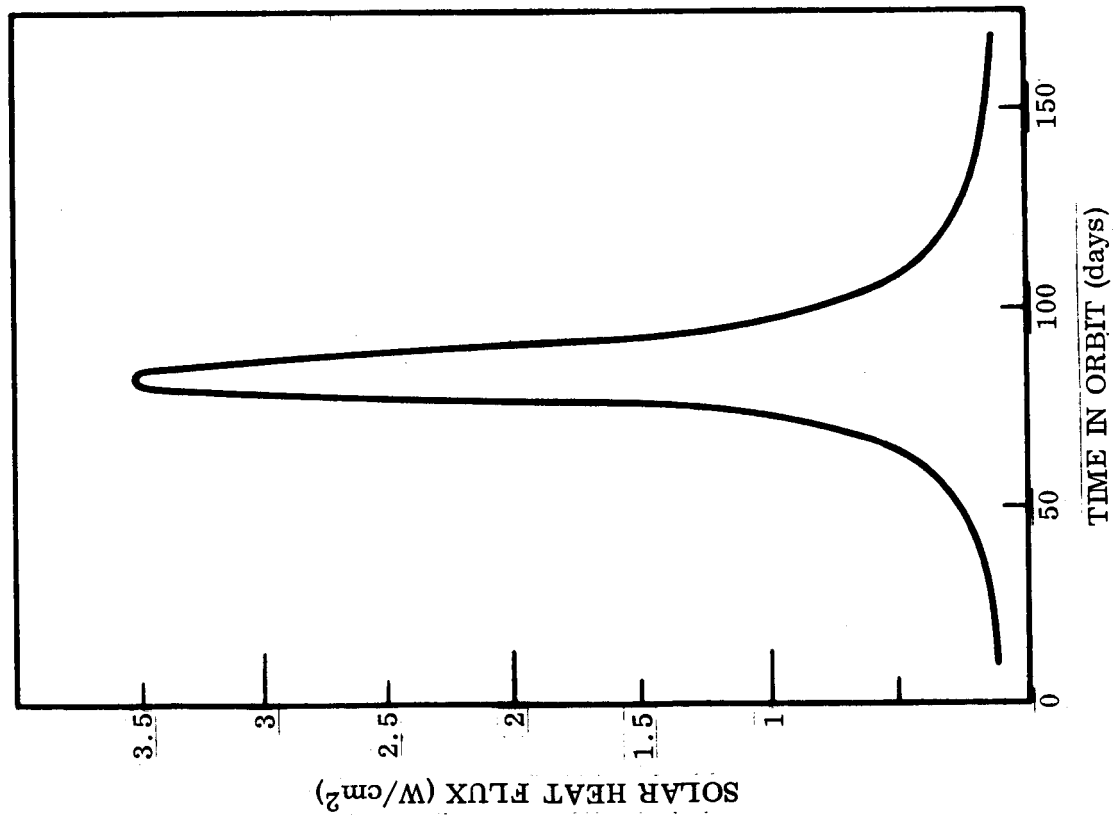
Figure 2 Solar Heat Flux on Flat Plate, 0.20 Perihelion Solar Probe

8
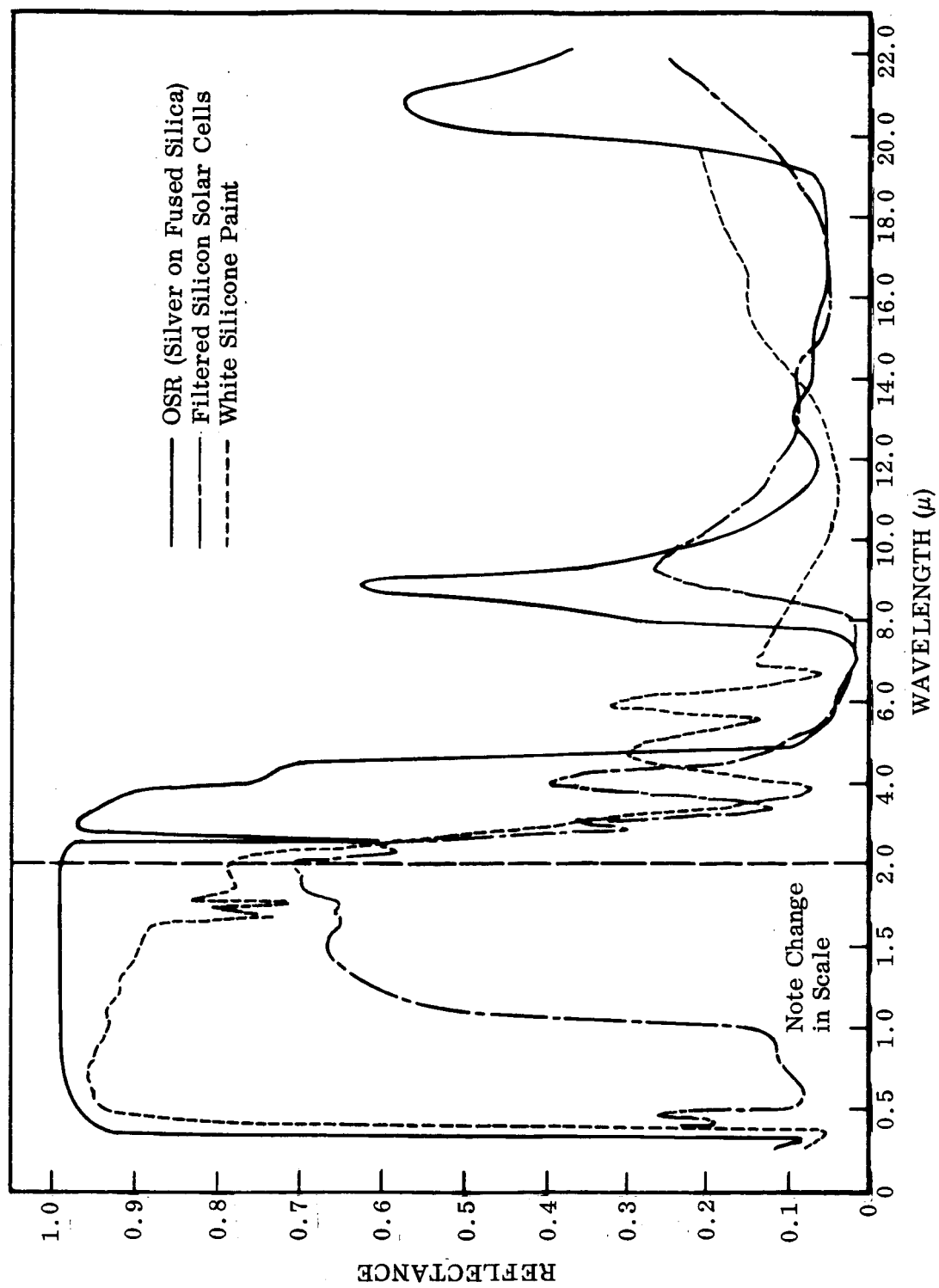
Figure 3 Spectral Reflectance of Spacecraft Surfaces
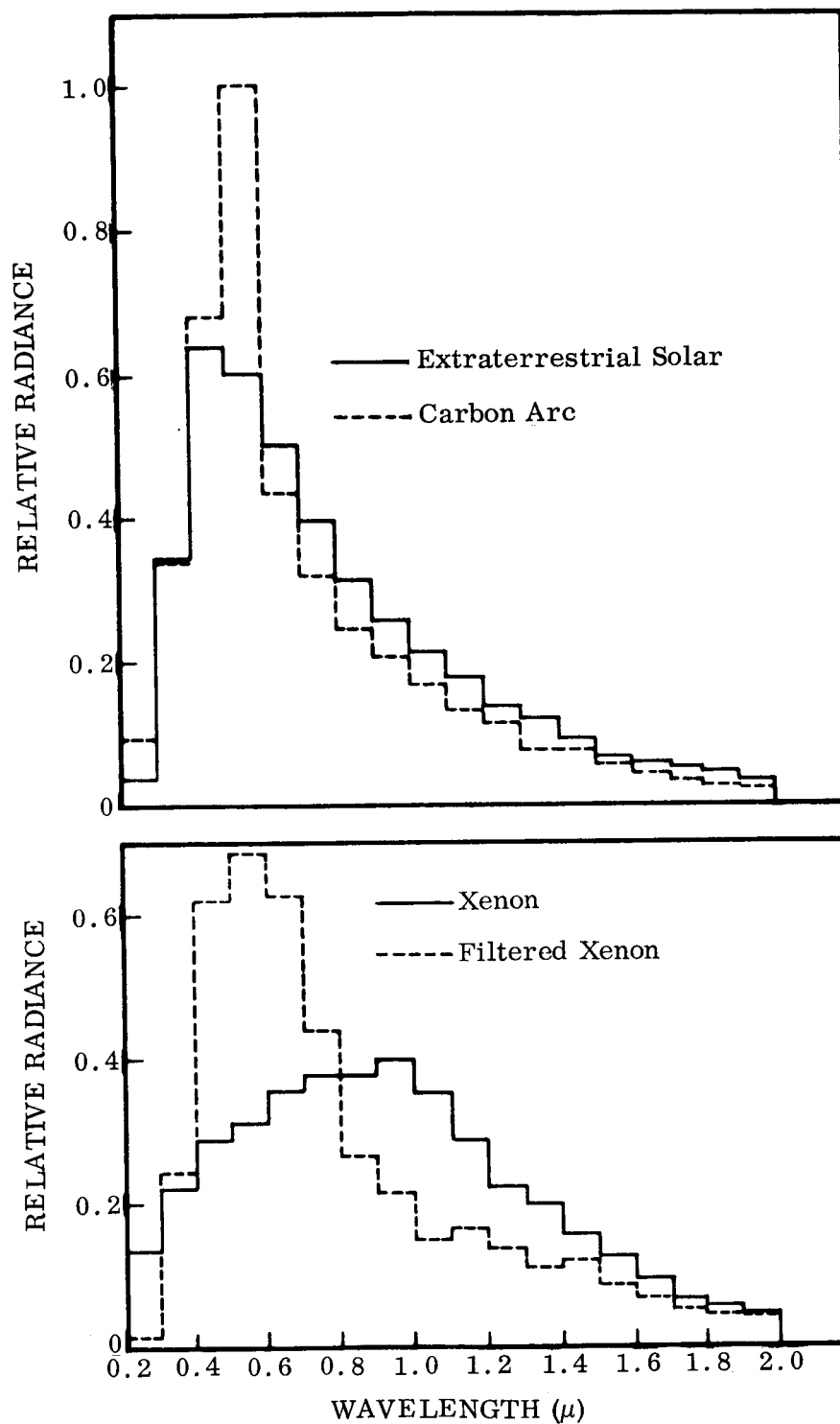
Figure 4 Relative Spectral Radiance of Several Sources Normalized
to Equal Total Energy Content

10

TABLE 1. – TEMPERATURE COMPARISONS OF MAJOR NODES COMPUTED
FOR VARIOUS ENERGY SOURCES[a]
(1-Sun Solar Constant, Temperature °K)

Node no.	Solar	Carbon arc	Xenon	Filtered xenon
9	198	198	198	198
10	304	304	306	305
11	304	304	305	305
12	285	285	285	286
15	206	206	206	206
16	214	214	214	214
22	208	207	210	208
23	182	182	184	183
25	278	277	284	280
27	286	284	294	288
32	167	168	165	162
34	147	147	144	140
35	197	197	197	197
38	288	288	294	290
40	326	325	336	330
41	276	275	280	278
43	339	338	349	343

[a]These results obtained for spacecraft using original thermal
analyzer computer model described in Appendix A.

TABLE 2. – TOTAL ABSORPTANCE OF OSR (CORNING 7940 FUSED SILICA
W/SILVER) AND FILTERED SILICON SOLAR CELL FOR VARIOUS
ENERGY SOURCES

Energy source	α OSR	α Solar cell
Solar	0.047	0.705
Carbon arc	0.048	0.692
Xenon	0.040	0.789
Filtered xenon	0.038	0.738
G.E. T3-500 tungsten lamp		
a. 40 V	0.033	0.49
b. 65 V	0.028	0.49
c. 90 V	0.025	0.51
d. 115 V	0.024	0.53

absorptance caused by shifts in the spectral distribution of incident energy. Table 2 presents values of total absorptance for the sources considered in the above computations and includes values for high-temperature tungsten filament lamps at various voltages. The tungsten absorptances were determined by integration of the spectral reflectance of the material with respect to the tungsten spectral radiance data shown in Figure 5.

The spectral distribution shown in Figure 5 was determined using a spectral calibration stand wherein monochromatic energy emitted from the tungsten source was compared to that emitted from an N.B.S. standard tungsten strip lamp. The comparison was made by alternately focusing each source on the inlet slits of an infrared single pass prism monochromator that was equipped with a vacuum thermocouple detector. The calibration apparatus utilized the same optics to view each source, a procedure which eliminates errors associated with different optical surfaces and path lengths. A comparison of the signals obtained from each source provides an absolute measure of the unknown spectral radiance under the assumption that the detection and amplification systems are linear. The procedure requires that the source image completely fill the monochromator entrance slits that are adjusted according to the spectral intensity from the source. Thus, equal emitting areas are compared and at no time is the viewed source width greater than 1 mm. The spectral irradiance presented in Figure 5 represents energy coming directly from the filament and the small area of quartz enclosure through which the filament is viewed. The considerable portion of infrared energy emitted by regions of the quartz enclosure that are not viewed by the monochromator are not accounted for by this procedure. Therefore, the results obtained for tungsten source absorptances from the data of Figure 5 are, at best, rough estimates of actual conditions.

The complexity of the spacecraft design with its extensive use of multilayer insulation makes it extremely difficult to construct an analytical computer model which adequately predicts thermal performance under the extreme environmental conditions of the proposed mission. Consequently, verification of acceptable thermal performance through laboratory testing of the spacecraft is highly desirable. However, the size of the spacecraft, its long booms and antennas, and its low α_s/ϵ thermal control surfaces require careful analytical and experimental investigation into potential testing techniques to ensure that meaningful simulation is accomplished.
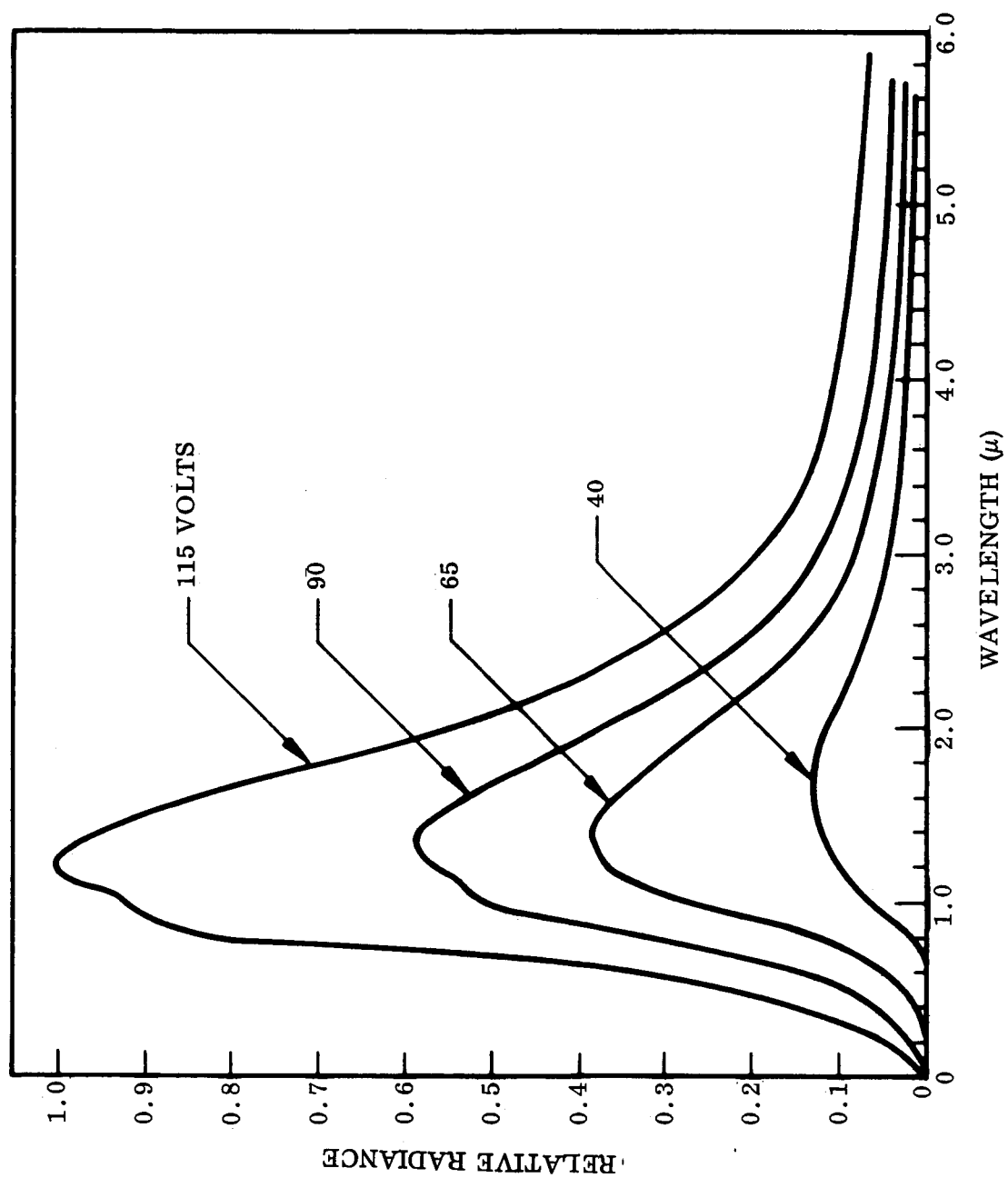
Figure 5   Relative Spectral Radiance of G. E. -Type T3-500 Quartz Lamp

Section 5

MODEL TEST PROGRAM

5.1 OBJECTIVE

The overall objective of the model program was to produce a test object that,
when subjected to simulated test conditions, would respond in a manner similar to
that anticipated for an advanced Pioneer spacecraft. A secondary objective was to
demonstrate the utility of the computer analyzer program for for predicting thermal
performance of the test object under simulated space conditions. These objectives
were met through the design and construction of a half-scale thermal model of the
spacecraft configuration described in the previous section. This model was tested
in a simulation chamber using a carbon arc solar simulator at 1 sun and high-
temperature tungsten filament lamps for total energy fluxes up to 9 suns.

5.2 MODEL DESIGN

The thermal model constructed during this program was designed to include all
of the major nodes and connecting resistances of the prototype spacecraft conceptual
design. However, it is important to note that the model could not be constructed to
match every detail of the final hardware. To construct an exact model of the pres-
ently conceived hardware was considered unnecessary within the context of the pro-
gram since a direct indication of prototype temperatures was not the primary
objective.

Wherever possible, the model was constructed in accordance with the thermal
modeling laws (refs. 10, 11); however, in some cases very high thermal resistances
could not be modeled due to the size and geometry involved. The following ground
rules were used as a basis for model design:

(1) Major thermal paths should match, as closely as possible, those of the
    proposed prototype configuration.

(2) External areas must have the same sensitivity to external sources as the
    prototype.

(3) Temperatures of the model should be on the same order as the prototype.

(4) The same multilayer insulation should be used in the model as is proposed
    for the prototype.

(5) Steady state modeling should be used.

14

(6) The size of the model should be approximately one-half that of the prototype.

(7) The design of the model should comply insofar as possible with the model laws for steady-state conditions,

$$\alpha * S * A_p^* = Q^* = \frac{K*A*T*}{L*} = \epsilon*A*T*^4$$

where asterisks designate ratios of properties between the model and prototype (i.e., $\alpha^* = \alpha_m/\alpha_p$).

These ground rules led to design of the model shown in Figure 6. Details of the surface coatings and connections are given in Table 3.

External surfaces on the model consisted of combinations of second surface reflectors (OSR), black Thermatrol* paint, and white Thermatrol paint. OSR and black Thermatrol were used exclusively to duplicate surfaces covered by solar cells and OSR on the prototype. The percent of coverage on each major zone was such that the α/ϵ for solar energy would be the same as the prototype and was determined from the spectral reflectance data on those surfaces. While the combination did preserve the ratio α/ϵ for solar energy, the average values of α and ϵ were not separately preserved. Therefore, while the average equilibrium temperatures achieved by the test model would be nearly the same as for the prototype, the relationship between internally generated energy and externally absorbed and emitted energy would not be preserved. White Thermatrol paint was used on the despun antenna and heat shield as a substitute for the OSR covering these surfaces on the prototype. This substitution simplified the construction and, since these elements were strongly decoupled from the body of the model, the differences in thermal level caused by the substitution were not considered serious. The reflectance spectrum of the surfaces used on the model are shown on Figure 7.

Internal design was accomplished to match as closely as possible the requirements of the modeling laws and the computer analyzer model that was constructed for the prototype. The required thermal resistances between the equipment platform and the upper and lower solar arrays were achieved. However, connections between the viewing band outer skin and equipment platform did not provide a resistance as high as that called for by the modeling laws due to the requirements of structural rigidity. The skin was constructed in four separate cylindrical sections to match the nodes of the computer model. These sections were made of 0.030-cm (0.012-in.) stainless steel sheet to preserve as much as possible the low thermal conductance of the prototype honeycomb skin. Internal energy dissipation was provided by three pairs of tungsten filament lamps contained within aluminum cubical enclosures that were fastened to the equipment platform at equally spaced locations. The equipment platform was constructed of 0.48 cm thick aluminum plate to assure a uniform distribution of energy over its entire surface.

---

*Thermatrol is a room-temperature curing silicone thermal control paint.

15

DIMENSIONS
IN CENTIMETERS
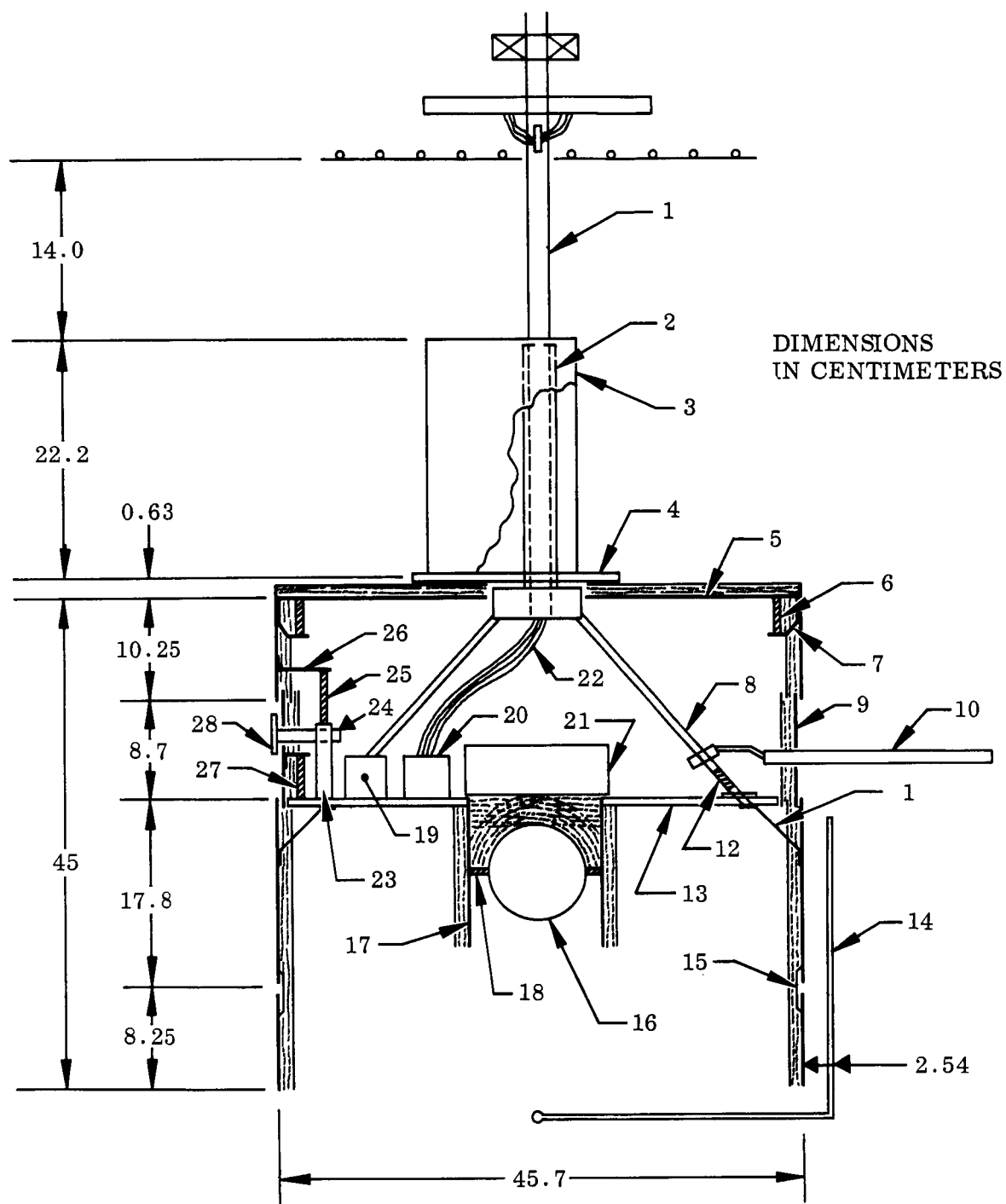
IDENTIFICATION NUMBERS
ARE GIVEN IN TABLE 3.

Figure 6 Test Model Design

16
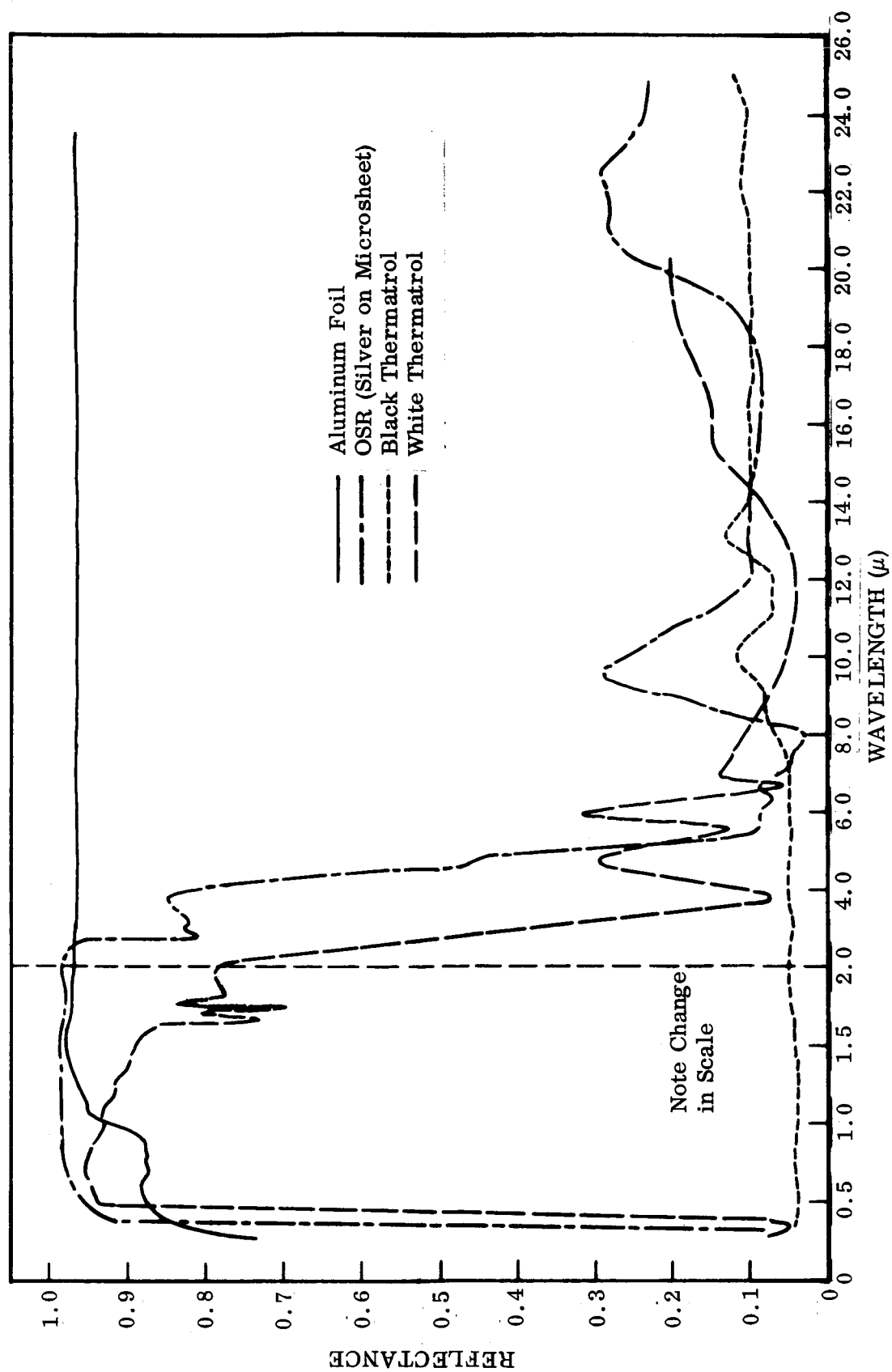
Figure 7 Spectral Reflectance of Model Surfaces

Aluminum Foil
OSR (Silver on Microsheet)
Black Thermatrol
White Thermatrol

Note Change
in Scale

WAVELENGTH (μ)

REFLECTANCE

18

TABLE 3. – PROPERTIES OF TEST MODEL STRUCTURE SHOWN ON FIGURE 6

Ident.[a] no.	No. used	Description[b,c]
1	1	Stainless-steel tube, 1.91 D × 0.0305 T
2	1	Aluminum tube, 2.86 D × 20.3 L × 0.165 T
3	1	Aluminum despun antenna, 20.3 D × 0.079 T
4	1	Aluminum plate, 25.4 D × 0.157 T
5	1	Stainless-steel top cover, 44.93 D × 0.0305 T, center hole – 6.99 D
6	4	Teflon support rod, 0.953 D × 5.08 L
7	4	Aluminum clips, 0.953 W × 4.65 L × 0.25 T
8	3	Stainless steel support tube, 1.27 D × 0.071 T
9		Multilayer insulation blanket – used on interior and exterior of model as shown by shadow
10	3	Aluminum boom, 0.953 H × 2.22 W × 17.75 L rectangular tubing, 0.236 T
11	8	Stainless steel support bracket, 4.83 L × 0.714 W × 0.63 T
12	3	Teflon rod spacer, 1.27 D × 0.635 L
13	1	Instrument platform, 44.93 D × 0.476 T aluminum plate
14	2	Lower array heat shield, aluminum 1/4 cylinder, 28.7 H × 0.089 T
15	10	Stainless steel joining clips, 3.25 L × 0.625 W × 0.0305 T
16	1	Copper sphere (hollow) 10.16 D, covered with polished aluminum
17	1	Stainless steel cylinder, 12.07 D × 11.4 H × 0.0305 T
18	4	Nylon support rods, 0.305 D × 0.953 L
19	3	Lamp box enclosure, aluminum, 6.99 × 5.40 × 4.13
20	1	Thermocouple reference junction box, aluminum, 6.99 × 5.40 × 4.13
21	1	Stainless steel cover cylinder, both ends closed, 12.7 D × 6.35 H
22	78	Leads from center support tube
23	6	Aluminum stand-off for support of upper array and sun sensors, 2.54 D × 6.16 L
24	4	Aluminum sun sensor support rod, 1.27 D × 2.54 L
25	6	Teflon upper array support rod, 1.27 D × 3.21 L
26	6	Aluminum clip, 0.953 W × 2.3 L × 0.25 T
27	6	Teflon viewing band support rod, 1.27 D × 3.18 L
28	4	Aluminum sun sensor plate, sized to block opening in viewing band, 0.157 T

[a]Identification numbers from Figure 6.

[b]Dimensions in centimeters.

[c]D = diameter   W = width
   T = thickness   H = height
   L = length

The viewing band of the model did not conform in exact geometry with that of the prototype. The view ports of the prototype consisted of various sizes and shapes that could not be directly duplicated on the model with satisfactory accuracy. Therefore, the ports on the model were scaled to conform in area with those of the prototype but were all rectangular in shape. Twelve openings were cut in the skin with identical openings cut in the multilayer insulation blanket that covered the interior of this region. Four of these openings were blocked by white Thermatrol-coated rectangular plates that were thermally grounded to the equipment platform. These painted surfaces simulated the sun sensor surfaces of the prototype. Five of the openings were blocked by a single layer of aluminum foil to simulate similar surfaces covering flight instrumentation. The remaining three openings were used for entry of the experiment booms. Details of the opening layout are shown on Figure 8.

The booms were not duplicated in their entirety on the model due to space limitations in the solar simulator. The thermal analyses of the prototype indicated that the booms would have a minor influence on the overall thermal performance of the prototype. Therefore, these were duplicated using short (17.8 cm long), rectangular (0.95 by 2.22 cm), OSR-covered booms that were designed to provide the general thermal effects of these appendages.

The despun antenna shield and despun lower array heat shield were constructed of aluminum sheet stock and conformed in shape to those proposed for the prototype. Both of these components were thermally isolated from the model by suspending them from framing within the simulation chamber rather than by direct attachment to the rotating model. This method of attachment failed to provide the required conduction paths; however, no other method of attachment was possible in view of the requirement that these components remain fixed within the simulation facility.

Thirty-five copper-constantan thermocouples were located throughout the model to provide temperature data on the performance of the model. They were located in accordance with the nodal network established for the thermal analyzer model and were placed in positions that were judged to give the best representation of the desired node. The reference junction for all thermocouples was a single enclosure located on the equipment platform. The temperature of this enclosure was determined from separate readings on two precision resistance thermometers that were located within the same enclosure. Copper leads from the reference junction were passed through a 40-pair slip ring assembly and brought out of the chamber through vacuum feedthroughs.

The completed model is shown in Figure 9. The general arrangement of the interior of the model is shown in Figure 10 where the insulation wrap, three support legs, lamp enclosures, and Teflon structural members can be seen.

Several difficulties were encountered during construction of the model that are worthy of consideration in terms of construction requirements for the prototype. These were primarily concerned with the attachment of OSR to the exterior surfaces and to the installation of the insulation blankets on the interior surfaces.
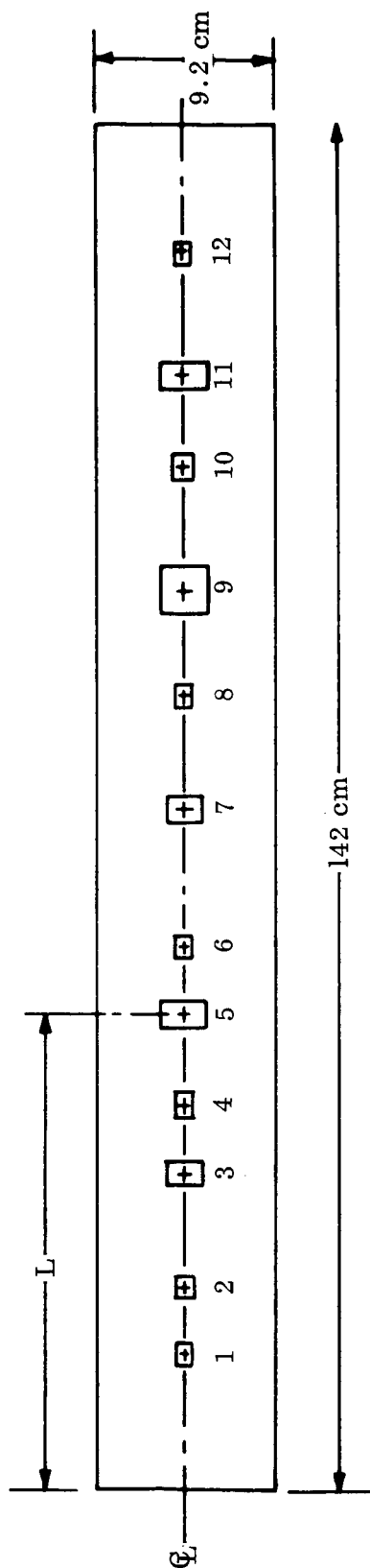
OPENING NO.	L (cm)	AREA (cm²)	DESCRIPTION
1	15.2	3.22	Blocked with Al foil
2	22.8	4.0	Sun sensor white plate
3	35.6	9.59	Blocked with Al foil
4	44.5	4.03	Boom opening
5	53.5	10.9	Sun sensor white plate
6	61.0	3.22	Sun sensor white plate
7	76.0	8.06	Blocked with Al foil
8	91.0	4.03	Boom opening
9	100.0	21.0	Blocked with Al foil
10	114.0	4.84	Sun sensor white plate
11	125.0	10.5	Blocked with Al foil
12	138.0	4.03	Boom opening

Figure 8 Viewing Band Layout for Penetrations
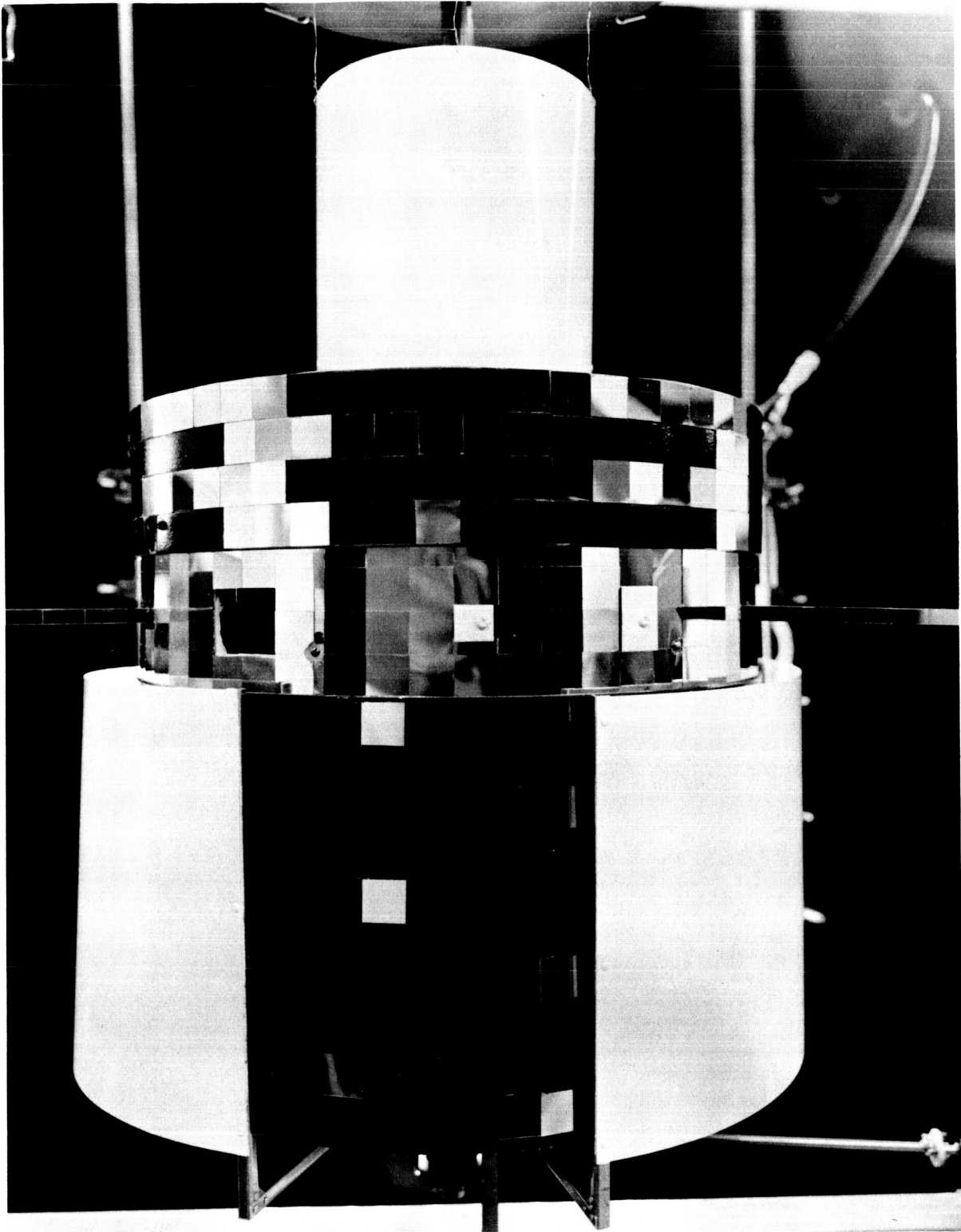
Figure 9 Thermal Model of Spacecraft
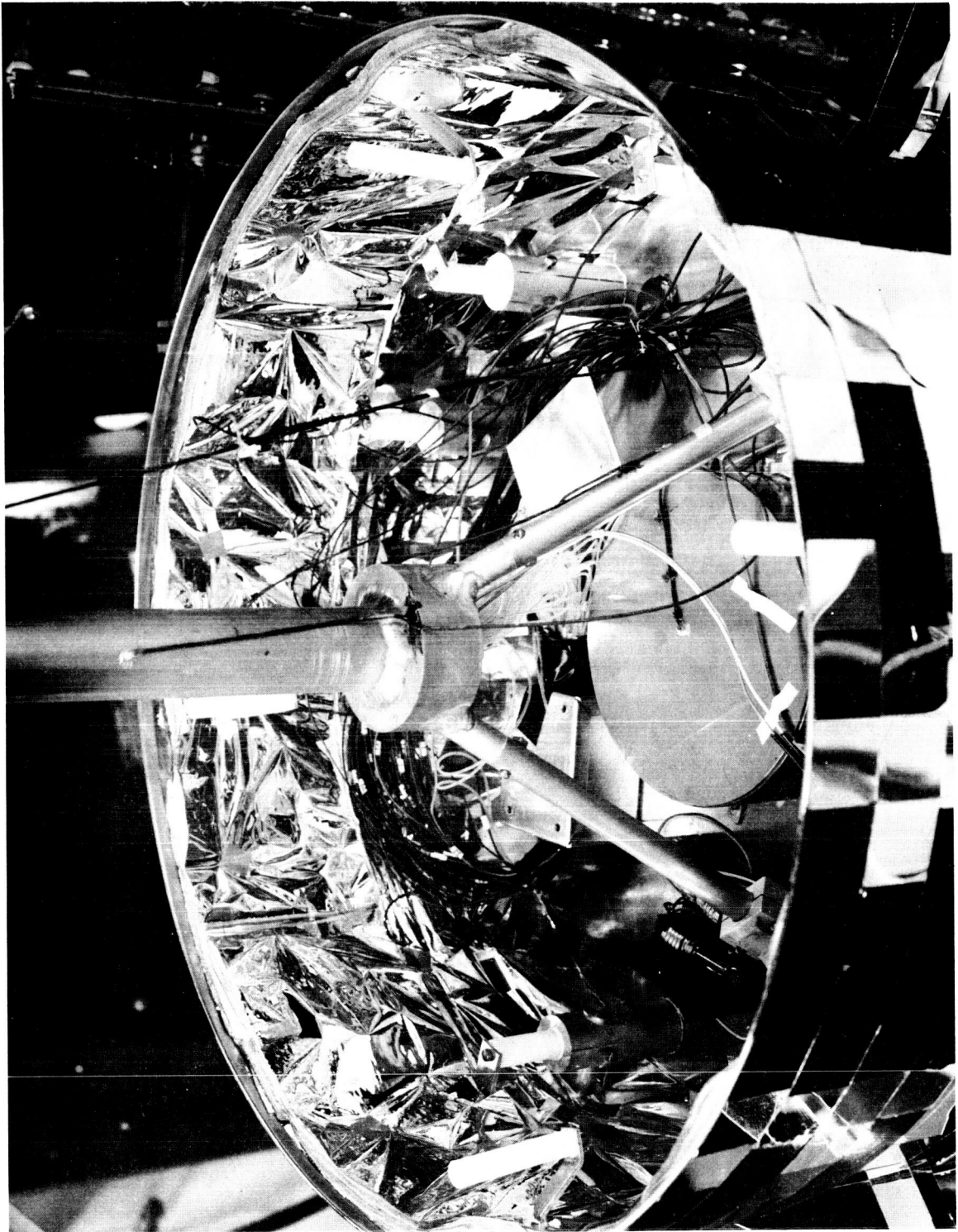
Figure 10 Thermal Model Interior

Several techniques were investigated for use in attachment of the 2.54 cm square OSR material (vacuum-deposited silver on microsheet). Direct application of OSR to the outer surface of the 46-cm-diameter cylinder using both single and double component high-temperature adhesives was attempted. The most promising adhesives found were General Electric Company RTV 102 and RTV 112 (both single component) and RTV 615 (two component). The single-component adhesives were sufficiently stiff to hold the mirror plates in place without slumping; however, upon high-temperature exposure (540°K), both of these materials caused considerable corrosion of the OSR mirror surface. This was apparently due to the acids used to promote hardening of these adhesives. The two-component RTV 615 was found to have desirable adhesion when fully cured and withstood high-temperature exposure without corrosion. However, this material is a very thin liquid when first applied and will not hold the mirrors in place on even a gently sloped surface.

Direct application of OSR mirrors to the cylindrical surface using RTV 615 would be a very lengthy process since the surface must be horizontal to avoid mirror movement during curing. This would limit each application to a single row on top of the cylinder. To speed up the process, it was necessary to establish a new application procedure where the mirrors were first bonded to a flexible backing in a horizontal position, and this assembly then applied to the cylinder. Both 1-mil polyimide film and 1/2-mil aluminum foil were investigated for use as backing materials. It was determined that either of these would provide satisfactory results using RTV 615 as the adhesive. A strong bond was achieved with mirror curvature closely conforming to that of the cylinder. A final decision was made to use the 1/2-mil aluminum foil for this application.

Following completion of the entire model, including preparation of all exterior surfaces except the booms, it was discovered that a new double-backed tape was available that held promise for attachment of the OSR to the outer surfaces. This tape consisted of polyimide film approximately 1 mil thick coated on both sides with high-temperature silicone adhesive. It was determined that attachment of the OSR using this tape was a much simpler process than that required using the adhesive and that reliability of the tape in maintaining a bond was much greater. This reliability was discovered during testing of the model which was subjected to thermal cycling from 195° to 534°K (-108° to 500°F). A number of the cemented OSR plates failed to survive these thermal cycles and were repaired using the double-backed tape. Additionally, the tape was used for application of all OSR surfaces on the booms. Throughout the entire test series there was not a single failure of surfaces applied with the tape.

The insulation blankets on the interior surfaces of the viewing band and lower array consisted of alternate layers of Dexiglas and double-aluminized Mylar. The upper array blanket was made of aluminized polyimide film in place of the Mylar since higher temperatures were anticipated for that region. These blankets were held together with 3-mil-diameter chromel wire that was spot welded to small stainless-steel tabs on the outside of the blanket. These blanket materials and attachment techniques are identical to those proposed for the prototype. Assembly into the model was accomplished by spot welding of the tabs to the model skin. It was

found that this method was inadequate due to numerous failures of the wire caused by the weight of the blanket. Additional tabs were installed in the blanket using 5-mil-diameter wire to provide greater strength. These additional wires alleviated the problem to some extent, although slippage of the blankets continued. It was finally necessary to employ polyimide tape at numerous locations to maintain the required blanket locations. Failures of the tape did not occur.

A third problem in model design arose during actual testing of the model. The interior of the despun heat shield for the lower array was initially insulated with multilayer insulation to provide the greatest possible isolation of this region from the external source. It was found during testing that the rotating model frequently came in contact with the blanket even though the initial clearance was on the order of 1.9 cm. Upon contact the blanket became intimately attached to the lower array and caused seizure of the entire rotating section. The reasons for initial contact were never determined and the problem remained even though the blanket was firmly attached to the shields. The difficulty was overcome only by removal of the blanket and substitution of a single layer of aluminum foil in its place. This experience provides a strong indication that use of a multilayer blanket in this region should be avoided on the spacecraft.

5.3 TEST PROGRAM

5.3.1 Chamber Installation

The model was tested in a 2.5-m-diameter by 3.1-m long vacuum chamber which is equipped with a blackened, liquid nitrogen cold wall. The assembled model was suspended by the center stainless-steel tube from a rotating mechanism consisting of two bearings, a flexible coupling, and a variable speed dc motor. The desired nominal rotational speed was 60 rpm although tests showed that speeds as low as 10 rpm caused no change in thermal performance. The entire assembly was attached to overhead framing from the chamber door as shown by Figure 11. The motor, suspension system, and slip ring assembly were shielded from the model by a blackened, liquid-nitrogen-cooled plate so that energy from these components would not irradiate the upper surfaces of the model. The lamp bank shown in Figure 11 was not the one used for actual tests.

Heating of the despun antenna and center post was accomplished using manually controlled tungsten filament lamps with reflectors that were mounted in close proximity to these components. These lamps were not used for the carbon arc tests.

The despun heat shield on the lower array was mounted to a set of gears that permitted opening and closing of the shields with relation to either of the sources used. The gears were in turn attached to framework within the chamber and were manually driven through a rotating vacuum feedthrough.

24
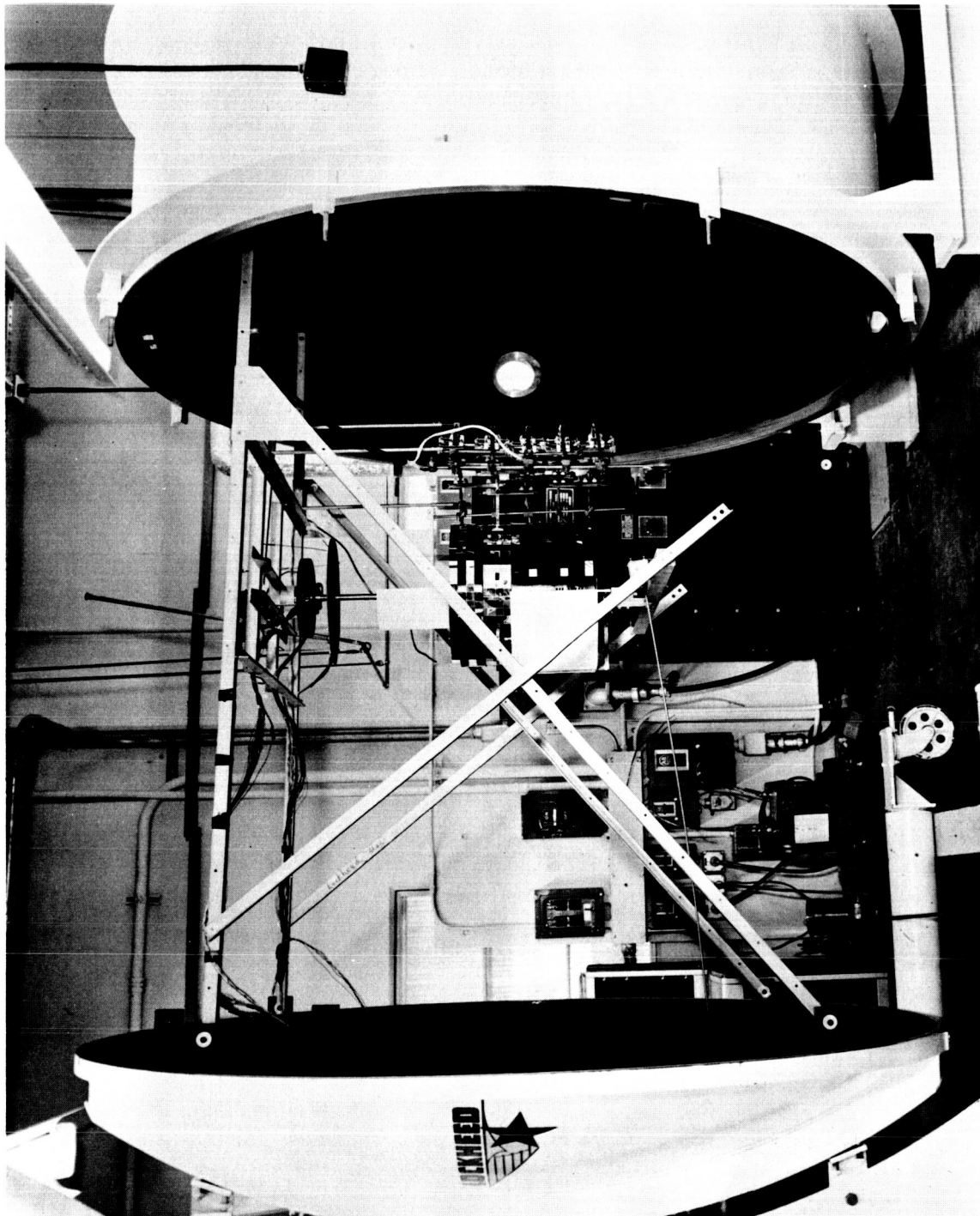
Figure 11 Chamber Installation of the Test Model

5.3.2 Carbon Arc

The carbon arc used was a commercially available unit with the capability of placing one solar constant over the entire model. Energy from the arc entered the chamber through a 30.4-cm-diameter by 2.54-cm-thick solar quality quartz window located 1.19 m from the frontal area of the model. Intensity of the beam was controlled through adjustment of movable lenses in the carbon arc nose-piece and monitored with black calorimeter disks.

5.3.3 Tungsten Lamp Bank

The lamps used were G. E. 500 T-3 units having a nominal rating of 500 W at 120 V. These are wound filament lamps and dissipate on the order of 100 W per linear inch of filament. The lamps were placed in front of commercially available gold-coated reflectors that directed energy from the lamp toward the test plane. The reflectors were sufficiently narrow so that only their edges could be seen when viewing the lamps from the front which limited cold wall blockage to a minimum. The individual lamp-reflector assemblies were attached by clips to solid copper conductors.

Several arrangements of the tungsten lamps were investigated. The first and simplest was to place the lamps in a single curved bank that placed the majority of energy from the bank on the vehicle. This arrangement is that shown on Figure 11. The top to bottom uniformity obtained from this bank was found to be very poor. In addition, stray energy from the bank impinged on areas of the model that would be in full shadow during actual simulated solar irradiation.

The poor results obtained with an open bank led to construction of a shield whose purpose was to direct energy from the lamps to the model with acceptable uniformity. The shield geometry reduced stray energy, increased the total flux striking the model, and led to greatly improved uniformity. The geometry of the shield is shown in Figure 12.

The shield was calibrated using several lamp arrangements, the most desirable one being that shown in Figure 12. Twenty-eight lamps were required to reach a total flux of 22 solar constants of energy at the test plane.

The lamp bank was calibrated for total intensity, for energy distribution above and below 5 μ, and for spatial distribution in the sample plane. The results of these calibrations are shown on Figures 13, 14, and Table 4.

The total energy falling on the test plane was determined through use of a specially fabricated water-cooled absorption calorimeter that was shaped to the exact dimensions of the model outer skin. The outer surface of the calorimeter was painted with black paint and the inner surface covered with several layers of aluminum foil. The calorimeter was mounted in front of the lamps at the exact location of the model

- Black Paint
- Polished Aluminum
- 28 Tungsten Filament Lamps

Shield Material:
Al Sheet, 0.159 cm thick
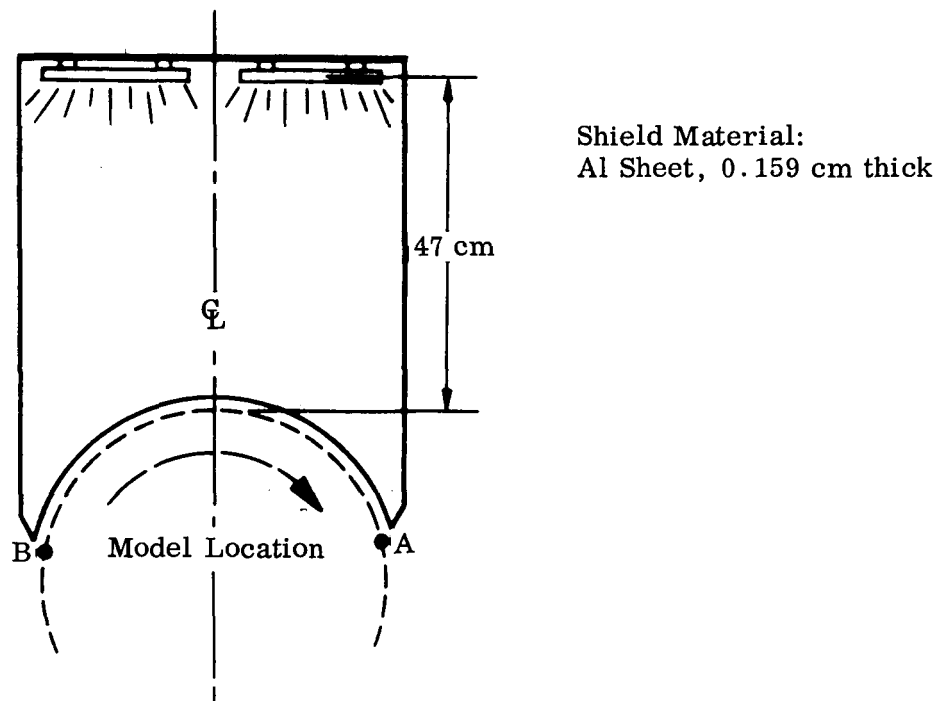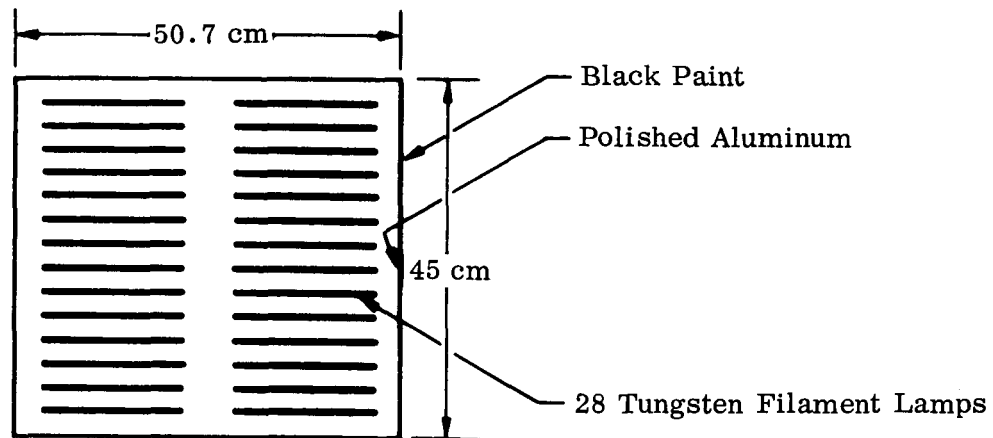
Figure 12 Lamp Bank and Shield Arrangement
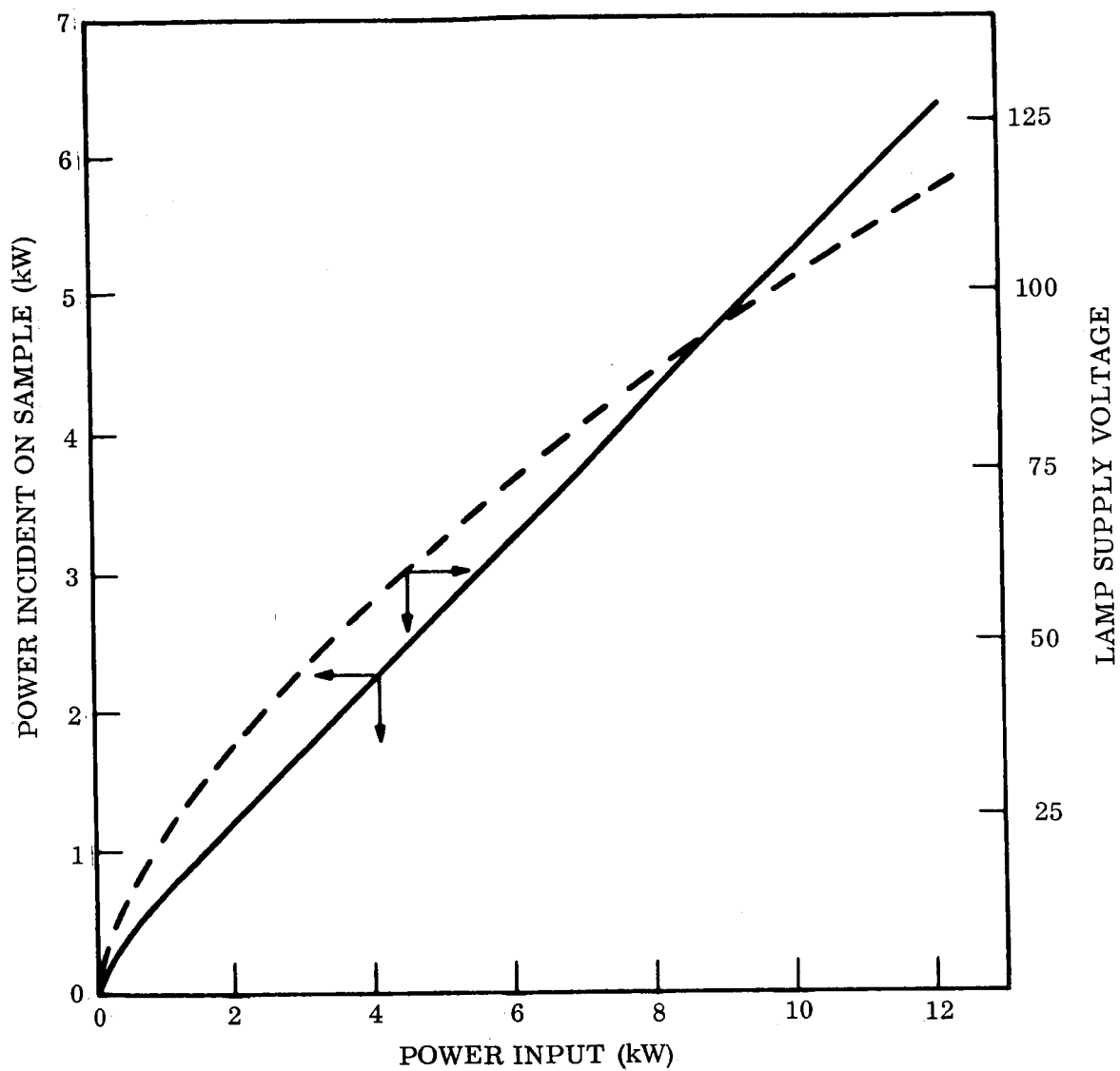
Figure 13 Tungsten Lamp Bank Total Intensities

0.0012	0.0744	0.506	0.874	0.848	0.945	0.989	0.936	0.859	0.799	0.119	0.020
.0012	.0565	.514	.881	.864	.976	.982	.949	.861	.786	.161	.017
.0012	.0726	.497	.857	.875	.979	1.01	.949	.850	.730	.194	.017
.0009	.1654	.531	.857	.910	.988	1.00	.946	.855	.718	.214	.015
.0009	.0696	.537	.890	.909	.992	1.00	.960	.883	.783	.217	.011
.0009	.0720	.542	.914	.917	.993	1.00	.979	.906	.827	.245	.009
.0009	.0905	.548	.932	.915	.993	1.00	.987	.926	.869	.167	.008
.0013	.0809	.537	.943	.924	.988	1.01	.986	.924	.863	.189	.008
.0017	.0672	.557	.869	.814	.854	.836	.863	.818	.796	.102	.009

A — B —

C_L

Top Edge

Bottom Edge

Figure 14 Relative Distribution of Energy Incident on Model Surface Facing Tungsten Lamp Bank With 28 Lamps

29

TABLE 4. − ENERGY DISTRIBUTION OF TUNGSTEN SOURCE

Source condition	Lamp voltage	Percent energy	
		Below 5 μ	Above 5 μ
Tungsten, 28 lamps			
0.9 sun	10.3	16	84
4.92 suns	40	42	58
9.0 suns	63	47	53
Tungsten, 6 lamps			
1.12 suns	34	51	49
4.22 suns	115	62	38

and determinations were made of incident power under vacuum conditions. The results of the calibration, shown on Figure 13, show that roughly 50% of the energy dissipated by the lamps is incident on the vehicle plane. The remainder of the energy is absorbed and re-emitted by the reflectors, absorbed, and re-emitted by the reflective shields, and lost through the clearance spaces around the calorimeter.

Distribution of energy flux on the test plane was determined by placing a water-cooled hemispherical radiometer in front of the lamp bank in numerous locations identical to those of the model surface. The radiometer was positioned at each location so that its receiving area was parallel to the surface of the test model. The relative distribution of the energy flux is shown in Figure 14 where each square represents an area of approximately 10 cm^2. This procedure accounted for the directional effects of the source arrangement as well as the curvature of the model plane. The results obtained showed that uniformity, except for the extreme top and bottom edges of the model, was within ±5%. Since the model would rotate past the source during actual testing, uniformity along the circumference of the test plane was not required. The total energy falling on the model obtained by integration of the distributional data compared to within 8% of that obtained from the water calorimeter tests. The agreement served to confirm that satisfactory results were achieved using the water calorimeter.

The spectral distribution of the lamp bank energy was not determined until the conclusion of the experimental runs. The measurement was made with the water-cooled hemispherical radiometer mounted in close proximity to the model skin. The system was placed into the simulation chamber under conditions identical to those used during the model test and a series of measurements was made with and without a quartz filter. The results obtained indicated the energy content above and below 5 μ. The spectral normal transmission of the window is shown in Figure 15 for wavelengths from 0.5 to 25 μ. The results of the calibration are given in Table 4
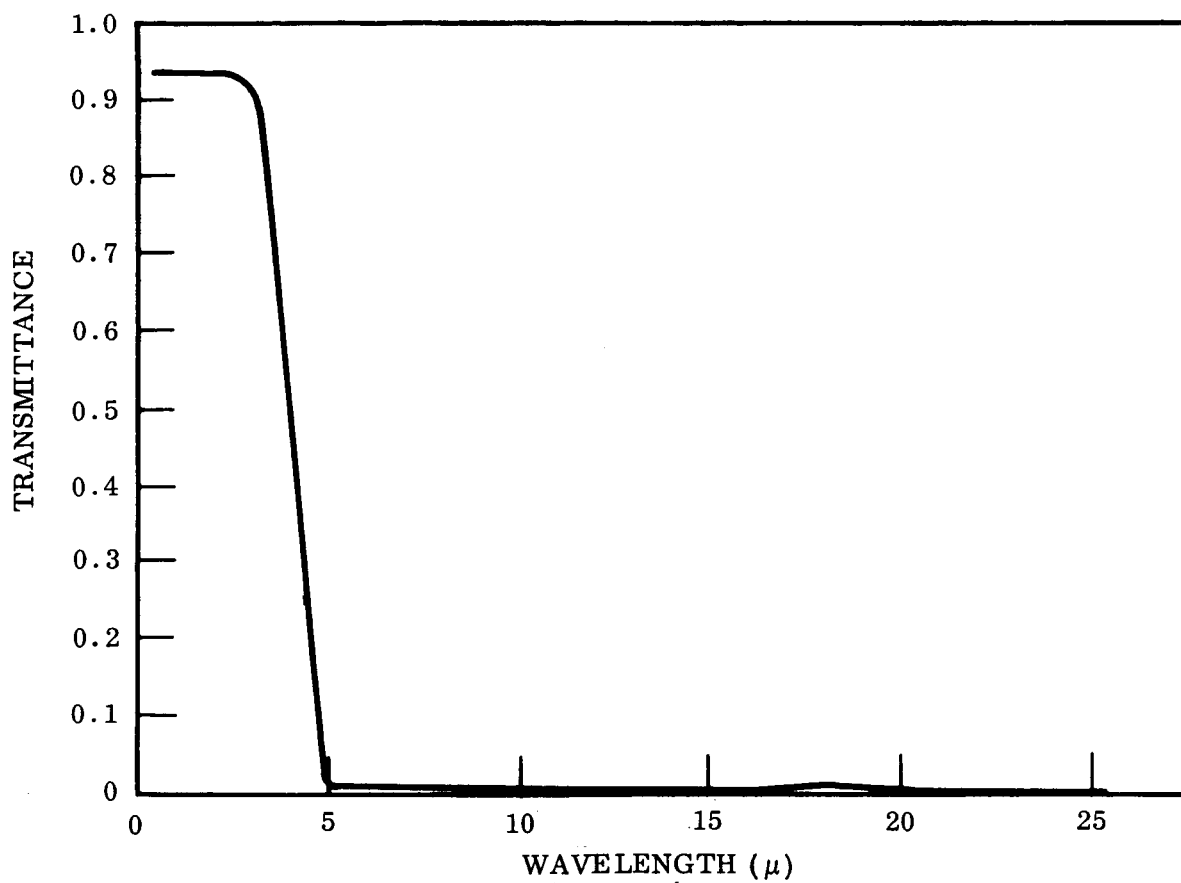
Figure 15 Spectral Normal Transmittance of Quartz Radiometer Window

and furnished the data required to determine the effective absorptances of the skin used in the analytical predictions of model performance.

5.3.4 Instrumentation

Instrumentation used to measure temperatures, voltages, power, and resistance was obtained from the LMSC Research Laboratory Loan Pool and was all of standard design. The performance characteristics of the instrumentation are given in Table 5. Each unit had an up-to-date calibration certification from the LMSC calibration laboratory and was within manufacturing specifications at the time of use.

TABLE 5. – INSTRUMENTATION

Type	Serial	Range	Precision or accuracy	Use
Wattmeter	MSL 65414	0−12 0−24 0−48	0.1 0.2 0.4	Internal power dissipation
A.C. null voltmeter	LMSC 77629	0−0.5 0−5 0−50	0.2% 0.2% 0.2%	Supply voltage to model internal sources
Resistance bridge	LMSC 77699	0.1−100 meg	0.1%	Reference temperature
A.C. voltmeter	MSL 65671	0−30 0−150 0−750	0.2 1 5	Tungsten source supply voltage
24 Pt. mV recorder	LMSC 78353	0−10	0.5	Monitor model performance
Portable mV potentiometer	MSL 54893	0−1020	0.05	Model thermo-couple response
Hemispherical radiometer	NASA/Ames A-79425	0−25 solar constants 5 mV/sun	−	Lamp bank calibration

5.3.5 Test Conditions

The model was tested in vacuum (2×10^{-6} mm Hg) using six variations of source irradiation. During these tests, certain regions of the model were allowed to establish their own equilibrium temperature while others were controlled during the experiment to provide required temperature levels. Table 6 presents the conditions used for each of the tests.

TABLE 6. – MODEL TEST CONDITIONS

Run no.	Source	Total incident flux (equivalent solar constants)	Internal power dissipation (W)	Equipment platform emittance	Heat-shield position	Model speed (rpm)	Controlled temperature node no.[a] (°K)				
							17	18	20	40	43
1	Carbon arc	1.04[b]	29.5	0.87	Full open	60	–	–	–	–	–
2	Tungsten, 28 lamps, 10.2 V	0.90	29.5	0.87	Full open	14	–	–	–	–	–
3	Tungsten, 28 lamps, 40 V	4.92	24	0.87	25% open	14	347	388	350	401	321
4	Tungsten, 28 lamps, 62 V	9.0	6	0.87	10% open	42	407	446	411	372	319
5	Tungsten, 6 lamps, 34 V	1.12	31	0.87	Full open	45	–	–	–	–	–
6	Tungsten, 6 lamps, 115 V	4.22	24.4	0.87	25% open	40	347	390	350	401	330

[a]Blank entries indicate that node temperature was not controlled.

[b]Does not include infrared energy incident on test model from miscellaneous structure within the test chamber.

33

The controlled temperatures were established by setting either the lower array heat shield opening or the tungsten lamps which irradiated the antenna and dipole system. For the shields, the setting was full open for 1 solar constant and adjusted at higher levels to limit the lower array to a maximum temperature of 361°K. For the dipole and antenna, the controlled temperatures were selected on the basis of predicted performance for space conditions. These predictions were established from manual computations which relied upon the preliminary computer analysis of the original prototype as a guide. This procedure led to disagreement between the predicted space (solar) temperatures of the model, as determined from the model computer analyzer program, and the actual test results. In view of the disagreement, the actual test temperatures were used as fixed inputs to the analyzer program for comparison of experimental and theoretical results of solar irradiation.

5.4 THERMAL ANALYZER MODEL

The thermal analyzer model, constructed for computer analysis of the half-scale test model, was basically the same as that constructed during the Phase I portion of the program for analysis of the spacecraft (Appendix A). Thermal conduction and radiation resistances were changed where necessary to correspond to the physical characteristics of the thermal test model. Several iterations were required to refine the analytical model, making it representative of the physical test model. All refinements were made at the 1.04-sun intensity level using energy inputs derived from the initial carbon arc test run. An iterative approach was utilized in conjunction with test results because of the many estimates required to establish initial values of conduction and radiation resistances. Uncertainties in resistance determinations resulted from inaccuracies connected with definition of material thermophysical properties, contact resistances, and radiative exchange of factors.

The analytical model was designed for solution by the LMSC Mark-5C Thermal Analyzer Computer Program (ref. 12) and consisted of the following characteristics:

- 37 nodes (Figure 16)

- 25 conduction resistors (Table 7)

- 38 radiation resistors (Table 8)

- 11 multilayer insulation resistors (Table 9)

- Various fixed boundary temperatures for the 11 environments considered (Table 10)

- 8 fixed boundary heat rates introduced into the analog network for the 11 environments considered:
    1 internal dissipation heat rate (Table 11)
    7 external surface absorbed heat rates from the various sources investigated (Table 12)

Figure 16 Node Locations for Half-Scale Test Model Thermal Analyzer Program

TABLE 7. – THERMAL CONDUCTION RESISTANCES FOR HALF-SCALE TEST MODEL ANALYSIS

Resistor no.	Description	Connecting nodes		Resistance value (°K/W)
		i	j	
Antenna group				
02	Dipole to dipole base	18	16	4.40
04	Reflector to reflector base	20	17	3.74
57	Support shaft to dipole base	19	16	4010.0
Instrument bay group				
33	Tripod support, upper	16	15	30.4
34	Tripod support, lower	15	9	38.2
38	Boom bracket	9	11	73.8
56	Instrumentation cables to platform	19	11	759.0
10	Top cover to connecting bracket	24	22	738.0
13	Connecting bracket to upper array	24	27	5.80
24	Upper array to sun sensor brackets	27	8	155.0
25	Sun sensors to brackets	28	8	0.801
26	Platform to sun sensor brackets	11	8	0.211
23	Viewing band to platform	34	11	138.0
36	Booms	36	35	1.05
37	Booms to boom brackets	35	9	2.64
39	Lamp housing to platform	4	11	0.211
60	Viewing band insulation to platform	32	11	138.0
Lower array group				
42	Platform to gas bottle cylinder	11	13	24.9
43	Gas bottle cylinder to gas bottle	13	2	149.0
58	Gas bottle insulation to platform	14	11	52.7
48	Platform to lower array	11	40	9.70
51	Lower array insulation	38	41	827.0
52	Lower array insulation	39	42	827.0
53	Lower array skin	40	43	114.0
59	Insulation to edge area	42	45	6.59

TABLE 8. – THERMAL RADIATION EXCHANGE FACTORS FOR HALF-SCALE TEST MODEL ANALYSIS

Resistor no.	Description	Connecting nodes i	j	$RADK_{ij}$ $\left(\dfrac{cm^2\ hr}{sec}\right)$	Radiative characteristics ϵ_i	ϵ_j	F_{ij}	A_i (cm²)
Surface group to cold wall and structure								
104	Top cover	23	1	0.1232×10^{-2}[a]	0.04	1.0	0.70	1354.5
105	Upper array	27	1	$.3383$	.83			1.0	1457.7
106	Sun sensors	28	1	$.6092 \times 10^{-2}$	.95		1.0	23.0
107	Aluminum foil	29	1	$.5836 \times 10^{-3}$	.04		1.0	52.4
108	Viewing band	34	1	$.2756$	.80		1.0	1122.3
109	Booms	36	1	$.4673 \times 10^{-1}$	.80		.6	356.7
110	Lower array, upper	40	1	$.3162$	.86		1.0	1270.7
111	Lower array, lower	43	1	$.1808$	.86		1.0	593.4
117	Lower array, bottom	45	1	$.2269 \times 10^{-1}$	.89		1.0	182.5
112	Lower array, lower	41	1	$.9300 \times 10^{-2}$	.04		.44	1180.4
113	Lower array, upper	38	1	$.1190 \times 10^{-1}$	.04		.21	2547.8
114	Cylinder	12	1	$.2511 \times 10^{-2}$	.04		1.0	451.5
115	Cylinder insulation	13	1	$.6557 \times 10^{-2}$	.13		.8	228.3
116	Gas bottle	02	1	$.1153 \times 10^{-2}$	.04		.8	129.0
131	Equipment platform	11	1	$.2418$	.87		.77	1373.9
Instrument bay group								
154	Lamp housing	4	0[b]	$.1937 \times 10^{-2}$	.06	1.0	1.0	116.1
155	Equipment platform	11	0	$.7161 \times 10^{-1}$	.20			1290.0
156	Tripod support	15	0	$.6371 \times 10^{-2}$	.15			152.2
157	Antenna support	16	0	$.8789 \times 10^{-3}$	.10			31.6
158	Top cover	22	0	$.5720 \times 10^{-1}$	.13			1580.3
159	Upper array	25	0	$.1623 \times 10^{-1}$	.04			1457.7
160	Aluminum foil	29	0	$.4999 \times 10^{-2}$	.04			52.3
161	Viewing band inside to platform	32	11	$.1737 \times 10^{-1}$	.04			1560.9
170	Platform to viewing band outside	11	34	$.1014 \times 10^{-1}$	.20			180.6
Antenna/top cover group								
148	Reflector base to top cover	17	23	$.1390 \times 10^{-3}$	.04	0.04	.97	283.8
149	Dipole to top cover	18	23	$.9184 \times 10^{-4}$	.87	.04	.05	290.3
153	Top cover to both sides of antenna shield	23 / 23	20 / 20	$.1981 \times 10^{-2}$	.04 / .04	.95 / .87	.10 / .05	1296.5 / 1296.5
Lower array group								
132	Platform to lower array	11	38	$.1395 \times 10^{-1}$	.87	.04	.05	1373.9
133	Platform to lower array	11	41	$.9300 \times 10^{-2}$	.87	.04	.03	1373.9
134	Platform to cylinder	11	12	$.5115 \times 10^{-2}$	.87	.04	.02	1373.9
167	Shield to lower array	44	40	$.3608 \times 10^{-1}$	.10	.86	1.0	1270.7
168	Shield to lower array	44	43	$.1674 \times 10^{-1}$	.10	.86	1.0	593.4

Resistor no.	Description	Connecting nodes i	j	$RADK_{ij}$ $\left(\dfrac{cm^2\ hr}{sec}\right)$	ϵ_i	ϵ_j	$F_{ij}A_i$	
Boom and shield group								
162	Boom to upper array	36	27	$.0336 \times 10^{-1}$	.80	.83	19.4	
163	Boom to viewing band	36	34	$.0344 \times 10^{-1}$		.80	19.4	
164	Boom to lower array	36	40	$.335 \times 10^{-1}$		.86	16.9	
165	Boom to lower array	36	43	$.0078 \times 10^{-1}$		.86	3.9	
166	Boom to shield	36	44	$.0430 \times 10^{-1}$		.92	20.8	
169	Lower array to viewing band	40	34	$.1660 \times 10^{-1}$	.86	.80	92.9	

[a] This value was found to be in error after analysis had been completed; it should have been 0.10×10^{-1}.
[b] Node 0 is a fictitious blackbody node that is utilized to collect and distribute energy to components within the upper compartment region.

TABLE 9. – MULTILAYER INSULATION THERMAL RESISTANCES FOR HALF-SCALE TEST MODEL ANALYSIS

Resistor no.	Description	Connecting nodes		Surface area (cm^2)	Number of layers[a]	Conductivity factor
		i	j			
189	Top cover	22	23	1581.	30	4.4
190	Upper array	25	26	1469.4	10	6.0
191	Upper array	26	27	1469.4	10	6.0
192	Viewing band	32	33	1125.3	10	5.7
193	Viewing band	33	34	1125.3	10	5.7
194	Gas bottle top	02	14	120.9	07	6.0
195	Gas bottle cylinder	12	13	455.7	30	3.2
196	Lower array, upper	38	39	2538.9	15	4.0
197	Lower array, upper	39	40	2538.9	15	4.0
198	Lower array, lower	41	42	1181.1	10	6.0
199	Lower array, lower	42	43	1181.1	10	6.0

[a]The number of layers used in the analysis does not necessarily correspond to the number of layers used on the test model.

TABLE 10. – CONSTANT BOUNDARY TEMPERATURES (°K) FOR HALF-SCALE
TEST MODEL ANALYSIS

Run no.	Description	Node								
		1	17	18	19	20	36	40	43	44
1A[a]	Carbon arc, 1.04 suns	78	229	238	266	232	–	–	–	242
2A	Tungsten, 28 lamps, 0.9 sun	78	216	253	266	219	277	–	–	283
3A	Tungsten, 28 lamps, 4.92 suns	78	347	388	339	350	376	361	320	–
4A	Tungsten, 28 lamps, 9.0 suns	78	406	446	400	411	430	372	318	–
5A	Tungsten, 6 lamps, 1.12 suns	78	198	228	260	202	268	–	–	283
6A	Tungsten, 6 lamps, 4.22 suns	78	347	390	339	350	344	361	330	–
7A	Solar, 1.04 suns	78	229	238	266	232	–	–	–	200
8A	Solar, 0.9 sun	78	222	229	266	228	–	–	–	200
9A	Solar, 4.92 suns	78	339	352	266	373	–	361	328	228
10A	Solar, 9.0 suns	78	396	411	266	434	–	361	328	324
11A	Solar, 25 suns	78	511	530	266	560	–	361	328	450

[a]The letter "A" denotes analytical computer runs.

TABLE 11. – INTERNAL POWER DISSIPATION FOR HALF-SCALE
MODEL THERMAL ANALYSIS

Run no.	Description	Power dissipation (W)
1A[a]	Carbon arc, 1.04 suns	29.5
2A	Tungsten, 28 lamps, 0.9 sun	29.5
3A	Tungsten, 28 lamps, 4.92 suns	24.0
4A	Tungsten, 28 lamps, 9.0 suns	6.0
5A	Tungsten, 6 lamps, 1.12 suns	31.0
6A	Tungsten, 6 lamps, 4.22 suns	24.4
7A	Solar, 1.04 suns	29.5
8A	Solar, 0.9 sun	29.5
9A	Solar, 4.92 suns	24.0
10A	Solar, 9.0 suns	6.0
11A	Solar, 25.0 suns	12.5

[a]The letter "A" denotes analytical computer runs.

TABLE 12. – ABSORPTANCES AND ABSORBED HEAT RATES USED FOR HALF-SCALE MODEL ANALYSIS

Run no.	Description	Upper array (node 27)		Sun sensors (node 28)		Al foil (node 29)		Viewing band (node 34)		Booms (node 36)		Lower array (node 40)		Lower array (node 43)	
		α^b	W	α^b	W	α^b	W	α^b	W	α^b	W	α^b	W	α^b	W
1A[a]	Carbon arc, 1.04 suns	0.41	28.6	0.19	0.217	0.11	0.286	0.17	9.21	0.41	1.92	0.83	100.8	0.83	46.3
2A	Tungsten, 28 lamps, 0.9 sun	0.76	44.5	.88	.815	.04	.085	.70	35.2	–	T[c]	.85	57.1	.85	40.1
3A	Tungsten, 28 lamps, 4.92 suns	0.66	208.6	.66	3.40	.04	.481	.51	143.0	–	T	–	T	–	T
4A	Tungsten, 28 lamps, 9.0 suns	0.63	367.7	.63	5.92	.04	.914	.46	239.4	–	T	–	T	–	T
5A	Tungsten, 6 lamps, 1.12 suns	0.61	44.8	.61	.706	.04	.109	.45	28.4	–	T	.84	106.9	.84	49.5
6A	Tungsten, 6 lamps, 4.22 suns	0.55	149	.48	2.1	.05	.498	.34	81.7	–	T	–	T	–	T
7A	Solar, 1.04 suns	0.37	24.6	.17	.176	.12	.286	.08	4.16	.06	0.158	.71	95.96	.71	44.5
8A	Solar, 0.9 sun	0.37	21.2	.17	.152	.12	.334	.08	3.59	.06	0.136	.71	82.6	.71	38.4
9A	Solar, 4.92 suns	0.37	116.5	.17	.835	.12	1.83	.06	21.1	.06	0.744	.71	452.1	.71	211.0
10A	Solar, 9.0 suns	0.37	214.5	.17	1.53	.12	3.37	.08	36.04	.06	1.37	.71	835.1	.71	388.2
11A	Solar, 25 suns	0.37	593.3	.17	4.25	.12	9.32	.08	97.3	.06	3.79	.71	2306.0	.71	1072.0

[a] The letter A denotes analytical computer runs.
[b] Absorptance computed by dividing the incident heat rate into the absorbed heat rate.
[c] T denotes inputs of temperature instead of heat rate.

40

Node designations for the half-scale test model were similar to those used for analyzing the full-scale spacecraft, with the following exceptions: (1) nodes 5, 6, 7, 21, 30, 31, and 37 were deleted from the program; (2) node 19 was changed to represent the top of the stainless steel tube that supported the model; (3) node 44 was added to represent the despun lower array heat shield; (4) node 45 was added to represent the exposed edge area of the lower array multilayer insulation; and (5) a fictitious node designated as "0" was added to collect, average, and distribute radiant energy among all the nodes within the upper equipment-bay enclosure, thus allowing simple handling of an otherwise complex radiative exchange network.

5.4.1 Conduction and Radiation Resistor Details

Conduction and radiation resistors for the test model analysis were employed as described in Appendix A for the spacecraft analyses. A number of conduction and radiation resistors were consolidated or deleted and some additional nodes defined in order to adapt the analytical model constructed during Phase I to the test-model design. Table 7 lists resistor designations, connecting nodes, and values used for the conduction resistors. Table 8 lists resistor designations, connecting nodes, values of radiation exchange factor, surface properties, geometric view factors, and surface areas used in calculation of the radiation resistors. The emittance of the bottom surface of the equipment platform was set at a constant 0.87 to coincide with the test model design. This deviated from the original analyses described in Appendix A where the emittance was varied from 0.10 to 0.75 depending on equipment platform temperature.

5.4.2 Multilayer Insulation Thermal Resistances

Energy exchange through the multilayer insulation blankets was calculated by a linearized relation which combines the radiation and conduction relations described in Appendix A. The equations used to calculate insulation thermal resistances are summarized below:

$$R_{MLI_{i-j}} = \cfrac{1}{\cfrac{Fac}{} \left(\cfrac{1}{R_{COND}} + \cfrac{1}{R_{RAD}} \right)}$$

$$\frac{1}{R_{COND}} = A \left(k' \frac{D}{n} \right) (T_i + T_j) \frac{W}{^\circ K}$$

$$\frac{1}{R_{RAD}} = A \left(\frac{\sigma F_{ij}}{10^4 \, n} \right) (T_i + T_j) \left(T_i^2 + T_j^2 \right) \frac{W}{^\circ K}$$

where

Fac conductivity factor to account for insulation degradation due to pene-
     trations and supports
A   surface area of insulation (cm^2)
n   number of insulation layers
D   packing density of insulation (layers/cm)
k'   an empirically determined constant = 1.49×10^{-10} W/cm °K^2
σ   Stefan–Boltzmann constant = 5.6697×10^{-8} W/m^2 °K^4
F   radiation exchange factor between layers

Packing density was assumed to be uniform throughout the model at D = 31.5 layers/cm. The radiation factor between layers was determined from the infinite parallel plate relation:

$$F_{ij} = \frac{1}{(1/\epsilon_i + 1/\epsilon_j - 1)}$$

with

$$\epsilon_i = \epsilon_j = 0.06$$

$$F_{ij} = 0.031$$

Table 9 lists A, n, and Fac for the insulation defined in the resistance network analysis. In some cases the number of insulation layers shown in the table is different than was the case for the actual test model. For the test model, all multilayer insulation blankets consisted of 30 layers, except for that covering the top of the gas bottle which consisted of 15 layers. A lesser number of layers was used in the analytical computations for some vehicle regions, along with the conductivity factor Fac, to represent an estimated degraded insulation system caused by penetration and/or edge losses.

5.4.3 Boundary Temperatures and Heat-Rates

To specify the boundary conditions for the analyses of the test model, it was necessary to define either external surface temperatures or absorbed heat rates from external sources. Wherever possible, absorbed heat rates were determined either from test measurements or theoretical analysis of true solar performance. In other cases, temperatures were specified from test results or analysis. Tables 10, 11, and 12, respectively, define the boundary temperatures, internal power dissipation, and surface-absorbed heat rates for the 11 cases analyzed. The absorptances and heat rates shown in Table 12 were determined from test data for Runs 1A through 6A and by computations using surface spectral reflectance characteristics and accepted solar radiance data for Runs 7A through 11A. The values of absorptances and heat rates shown for the carbon arc run are higher than those given for the corresponding solar run. These increased values account for the low level infrared energy supplied to the test model by miscellaneous structure within the test chamber during the carbon arc run. The analysis for prediction of solar performance assumes that no sources of infrared energy are present.

42

Section 6

RESULTS

The results obtained from the experimental and analytical program are presented separately in Tables 13 through 17. In each case the node numbers used for identification are located as shown on Figure 16 of the computer analyzer program. Additional information on the source condition and total incident flux is also included.

Table 13 presents the steady state temperatures measured on the test model during exposure to six separate source conditions. The rotational speeds, internal dissipation rates, lamp voltages, and other parameters controlled during each of the tests were previously presented in Tables 4, 5, and 6

Table 14 presents the results obtained from the computer analyzer program for the same boundary conditions as were used for the chamber tests. Run numbers 1A through 6A are directly comparable to experimental run numbers 1 through 6. The external boundary conditions used for the predictions were established on the basis of experimental observations. Comparison of Table 14 with Table 13 provides an indication of the ability of the computer analyzer program to predict actual thermal performance.

Table 15 indicates the steady state temperatures that would be experienced by the model upon direct illumination by the extraterrestrial sun. These results were obtained using the computer analyzer program in conjunction with computed surface absorption rates for solar exposure. They do not include the effects of energy inputs from infrared sources such as the chamber windows, model support structure, and lamp bank reflectors, but do assume a background temperature equivalent to that of the liquid-nitrogen-cooled chamber walls. Therefore, these results represent the performance expected for high quality solar simulation with nitrogen-cooled surroundings.

The differences between the various analytical and experimental results are principally due to changes in the effective total absorptance of the model surfaces when exposed to the simulation sources. Table 16 presents effective values of the ratio α/ϵ for the source conditions used. These were determined from data on the spectral reflectance of the materials and the energy distribution during the test.

The average internal temperatures achieved during the tests were affected both by changes in external boundary conditions and by the performance of the multilayer insulation blankets. Table 17 presents the values obtained for the thermal conductivity of the individual blankets. These values were computed from the analytically predicted performance presented in Table 14 and not from the experimental results presented in Table 13. Therefore, the accuracy of the results must be judged in terms of the agreement between predicted and observed performance.

43

TABLE 13. MEASURED MODEL PERFORMANCE, TEMPERATURE °K

Node number	Run number					
	1	2	3	4	5	6
	Source					
	Carbon arc	Tungsten 28 lamps	Tungsten 28 lamps	Tungsten 28 lamps	Tungsten 6 lamps	Tungsten 6 lamps
	Solar constants					
	1.04	0.90	4.92	9.0	1.12	4.22
1	78	78	78	78	78	78
2	258	266	254	251	257	247
3	272	283	303	332	288	306
4	302	—^{a}	—	—	—	—
8	278	284	298	308	289	300
9	238	272	366	411	266	340
10 & 11	279	282	298	310	289	300
12	246	244	265	283	248	277
13	268	271	282	294	277	286
14	272	283	296	320	286	301
15	246	270	358	396	264	348
16	238	253	368	418	246	370
17	228	216	346	406	198	347
18	238	253	388	446	228	390
19	266	266	255	272	261	267
22	268	282	324	361	284	323
23	246	230	272	310	220	274
25	271	285	338	374	286	330
27	260	282	416	482	277	387
28	282	287	310	330	293	310
32	274	286	333	364	290	325
34	230	278	386	434	264	336
36	239	277	376	430	268	344
38	255	251	272	288	258	276
40	336	324	361	370	334	364
41	249	241	259	276	246	262
43	322	302	320	318	311	330
44	264	182	550	660	185	519

^{a}Thermocouple failure, test runs 2 through 6.

TABLE 14. – COMPUTED MODEL PERFORMANCE, TEMPERATURE °K

Node number	Run number					
	1A[a]	2A	3A	4A	5A	6A
	Source					
	Carbon arc	Tungsten 28 lamps	Tungsten 28 lamps	Tungsten 28 lamps	Tungsten 6 lamps	Tungsten 6 lamps
	Solar constants					
	1.04	0.90	4.92	9.0	1.12	4.22
0	277	280	317	326	284	306
1	78	78	78	78	78	78
2	254	257	269	263	260	262
4	286	289	304	293	293	296
8	280	283	300	293	287	290
9	244	276	372	421	267	342
10 & 11	280	283	300	292	287	290
12	254	257	272	264	260	264
13	263	265	278	272	268	271
14	278	280	296	289	284	288
15	246	267	307	400	252	351
16	239	254	384	438	230	384
17	228	216	347	406	198	347
18	238	253	382	446	228	390
19	244	267	338	400	260	338
20	231	219	350	411	202	350
22	275	279	318	329	282	306
23	244	244	328	354	241	311
24	254	284	415	478	284	381
25	272	282	346	376	284	328
26	264	282	386	436	284	357
27	254	284	416	479	284	382
28	279	283	302	297	287	290
29	297	282	340	368	286	332
32	274	284	318	328	285	300
33	252	284	362	398	279	325
34	226	285	394	446	274	346
35	242	277	375	428	268	344
36	242	277	376	430	286	344
38	258	258	276	274	264	270
39	302	296	323	330	309	324
40	337	328	360	372	345	364
41	238	238	250	245	244	246
42	235	237	242	240	246	246
43	325	318	320	318	335	330
44	242	283	—	—	283	—
45	232	228	233	231	238	236

[a] Temperatures include effect of low-level infrared energy absorption from miscellaneous structure within test chamber.

45

TABLE 15. – COMPUTED MODEL PERFORMANCE FOR SOLAR IRRADIATION, TEMPERATURE °K

Node no.	Solar constants				
	1.04	0.90	4.92	9.0	25.0
0	274	271	298	300	364
1	78	78	78	78	78
2	253	251	257	241	268
4	284	281	288	263	300
8	277	275	283	262	299
9	222	218	260	281	344
10 & 11	278	275	283	261	298
12	252	250	272	238	270
13	260	258	265	248	277
14	276	273	280	260	295
15	236	230	306	337	413
16	238	230	346	400	512
17	228	222	338	396	511
18	238	229	352	411	530
19	266	266	266	266	266
20	231	228	373	434	562
22	272	269	300	304	370
23	242	239	319	358	460
24	246	237	359	417	538
25	268	364	314	337	420
26	257	251	338	383	490
27	246	237	359	418	540
28	277	274	283	330	301
29	294	289	371	413	525
32	270	267	279	266	310
33	242	238	269	277	338
34	204	197	257	288	362
35	219	212	256	278	341
36	218	214	254	277	340
38	255	251	266	254	274
39	298	288	320	317	323
40	332	320	360	360	360
41	237	232	241	228	250
42	239	232	238	235	245
43	322	311	328	328	328
44	200	200	228	324	450
45	230	224	234	232	236

TABLE 16. – EFFECTIVE α/ϵ OF MAJOR SECTIONS FOR VARIOUS SOURCE CONDITIONS

Source condition	Surface		
	Upper array	Viewing band	Lower array
Solar	0.45	0.10	0.84
Carbon arc	.45[a]	.10[a]	.84[a]
Tungsten, 28 lamps			
0.90 sun	.92	.87	1.0
4.92 suns	.79	.64	.99
9.0 suns	.76	.58	.98
Tungsten, 6 lamps			
1.12 suns	.74	.56	.99
4.22 suns	.66	.43	.98

[a]These values are for carbon arc irradiance only and do not account for the presence of low-level infrared energy sources within the test chamber during the 1.04-sun carbon arc run.

TABLE 17. – EFFECTIVE THERMAL CONDUCTIVITY OF MULTILAYER INSULATION DETERMINED FROM HALF-SCALE MODEL COMPUTER ANALYSIS

Location	Carbon arc 1.04 suns (W/cm °K)	Tungsten 4.22 suns (W/cm °K)	Tungsten 9.0 suns (W/cm °K)	Solar 25 suns (W/cm °K)
Upper array	6.58×10^{-6}	1.42×10^{-5}	2.39×10^{-5}	3.29×10^{-5}
Viewing band	5.55×10^{-6}	1.05×10^{-5}	1.73×10^{-5}	1.16×10^{-5}
Lower array, upper	3.98×10^{-6}	4.85×10^{-6}	5.02×10^{-6}	4.85×10^{-6}
Lower array, lower	6.23×10^{-6}	6.75×10^{-6}	6.4×10^{-6}	6.75×10^{-6}
Top cover	1.56×10^{-6}	2.77×10^{-6}	3.12×10^{-6}	5.37×10^{-6}
Gas bottle cylinder	1.12×10^{-6}	1.21×10^{-6}	1.21×10^{-6}	1.3×10^{-6}
Gas bottle top	1.44×10^{-5}	1.56×10^{-5}	1.58×10^{-5}	1.66×10^{-5}

Section 7

DISCUSSION OF HALF-SCALE MODEL PERFORMANCE

An evaluation of the results presented in the previous section requires that all thermal influences be considered in terms of their effect on the measured and computed temperatures. A direct comparison of temperatures alone is inadequate for interpretation, since the system itself changes characteristics as the temperature range is varied. The important variables are an increase in thermal conductance of the insulating blankets with increasing temperature, variations in internally dissipated energy during the test series, and changes in source spectrum from one equilibrium condition to the next.

An overall evaluation of the results indicates that in all cases where the model was tested with tungsten lamp energy, the surfaces covered with OSR experienced considerable overheating relative to that expected for solar energy. The excess energy absorbed by these surfaces increased the thermal level of the entire test model. This is adequately demonstrated by comparison of 1 solar constant results presented in Table 13. Node 34, the viewing band exterior, achieved an equilibrium temperature of 230°K under carbon-arc simulation. The same node increased to 278°K under tungsten simulation using the 28 lamp bank even though the tungsten bank was run at 0.9 solar constants rather than 1.04 as was the case for the carbon arc. At this level, the large lamp bank was running at very low voltage with most of the energy emitted being at wavelengths in excess of 5 μ. The 1 solar constant results obtained with the 6 lamp tungsten source lowered the temperature of node 34 to 265°K with a total irradiation of 1.12 solar constants. This represented an improvement due to the higher filament temperatures used; however, satisfactory simulation was still not achieved. A similar comparison for the remaining nodes and test conditions substantiates the observation that direct use of tungsten filament lamps results in excess absorption of infrared energy.

The infrared content of the lamp banks used to test the model substantially modifies the distribution of absorbed energy on the major surface zones of the spacecraft. This is more clearly shown by the computed values of α/ϵ presented in Table 16. The solar and carbon arc ratios are identical for the surface design used on the test model. However, the ratios computed for all arrangements and operating conditions of the tungsten lamps are considerably greater. Not only is there an increase in absolute value of the ratios, but more importantly, the differences in the ratio from one section of the outer surface to the other were altered. The effects of this alteration on the thermal performance are shown by the absorbed heat rates given in Table 12. For example, the absorbed heat rate into the OSR covered viewing band (node 34) for the 9-sun tungsten run was approximately 2.5 times that predicted for 25 suns of solar irradiation. These absorbed heat rates lead directly to transmission of energy to the interior of the vehicle as well as heating of the outer skin and

insulation. The elevated temperatures cause changes in thermal properties of the insulating materials that lead to even larger heat leaks to the interior of the spacecraft.

The results obtained at higher flux levels show that the higher tungsten lamp voltages and filament temperatures result in a lowering of the α/ϵ ratio. However, the values achieved are still entirely unacceptable for proper performance testing of the vehicle. The lowest α/ϵ ratio achieved for OSR covered surfaces was 0.43 using six lamps at maximum voltage. This would undoubtedly be further reduced by cooling of the lamp shield with liquid nitrogen; however, a reduction to acceptable levels would require complete removal of all energy beyond approximately 4.5 μ. While the lamp shields account for a portion of this energy, it is obvious that the lamp enclosures themselves are the primary source of infrared emission to the model.

The results obtained from the analytical model confirmed the experimental observations. A comparison of temperatures in Tables 13 and 14 for the same source conditions shows that at the low energy levels the analytical predictions compared favorably with the measured temperatures. As the incident flux was increased, the comparisons obtained were not as satisfactory. The computer model is apparently not sufficiently sensitive to thermally induced changes in properties to provide satisfactory high-temperature predictions. However, in spite of the disagreement at the higher temperatures, the computed results do provide an excellent indication of the performance trends caused by changes in external boundary conditions.

Computations were also made assuming that the model was exposed to true solar energy. The results of this computation are shown on Table 15 and, when compared to the results in Table 14, give an excellent measure of the thermal errors caused by use of the tungsten lamps. It is of interest to note that filtering of all energy beyond 4.5 μ would significantly reduce the thermal errors experienced by the test model. This would also be the case for the prototype spacecraft where the OSR and black paint surfaces of the model are replaced by OSR and solar cells. A computation of anticipated temperatures for the spacecraft using well filtered tungsten energy was not completed, but the spectral reflectance properties of the major surfaces lead directly to this conclusion.

The difficulty experienced in properly predicting the model performance by use of the computer analyzer program can be attributed to two contributing factors. The first is that the computer model was built using a minimum number of nodes so that the major influences of external sources would be readily evident to the analyst. A larger number of nodes could easily have been used to obtain greater accuracy; however, an evaluation of the influence of changing boundary conditions would have been considerably more difficult with the more complex network. The second reason for prediction inaccuracies is that of changing thermal properties of internal components. These are demonstrated to some extent by the data presented in Table 17 where the effective thermal conductivity of the insulating blankets is given for various test conditions. The values in the table were determined from the temperatures and heat rates obtained from the computer results. A comparison of the temperatures in Tables 13 and 14 for the multilayer insulation shows that the predicted gradients for

the blankets are in most cases in reasonable agreement with the measured gradients. This leads to the supposition that the conductivities obtained from the computation are within reasonable limits of those actually experienced by the test model. However, the values of conductivity for the blankets alone are not an adequate measure of agreement between the computer and test models. The energy entering the vehicle interior around penetrations, between adjacent blankets, and degradation of the blankets due to penetrations were only roughly estimated in the analyses. The influences of these unknowns on the overall performance of the test model cannot be clearly stated or introduced into the analytical model.

Section 8
TESTING TECHNIQUES FOR FLIGHT HARDWARE

The analytical and experimental results obtained from the half-scale thermal model show conclusively that testing of the advanced Pioneer spacecraft cannot be accomplished by direct use of tungsten filament lamps. The infrared energy emitted by the lamps results in excessive and improperly distributed energy absorption on the vehicle surfaces. Implementation of one of the following approaches is required to circumvent this difficulty:

(1) Use of simulated solar energy from a carbon arc or filtered xenon arc source

(2) Use of filtered tungsten energy over the entire cylindrical body with separate irradiation of the antenna

(3) Zonal heating of the cylindrical body with unfiltered tungsten energy and separate irradiation of the antenna

The analytical results obtained during Phase I of the program indicated that either filtered xenon or carbon arc energy could be used in the first method. The low temperatures achieved by the half-scale model under 1 solar constant of carbon arc energy further substantiated this finding. Therefore, the difficulty with this approach is entirely economical rather than technical. The development of a 25 solar constant simulator is within the present state-of-the-art, but would undoubtedly require very substantial funding and increase test costs to undesirable levels. However, it is obvious that the use of well collimated simulated solar energy would result in the best indication of actual flight performance.

The other approaches utilize tungsten filament lamps as a source and would result in considerably reduced equipment and operational costs. It can also be anticipated that the reliability of the equipment for extended operation would be increased. However, these approaches rely to some extent on either absorbed flux or temperature simulation as dictated by analytical predictions of flight performance.

The second approach requires the use of either filters or absorbers to eliminate far-infrared energy from the tungsten sources. Two possibilities are considered as promising. The first is the use of liquid-nitrogen-cooled, second-surface mirrors between the source bank and the spacecraft. A possible test arrangement is shown in Figure 17. The mirrors would act as effective absorbers for energy at wavelengths beyond 4.5 μ, while efficiently reflecting energy at the shorter wavelengths. For silvered second-surface quartz mirrors, the reflectance would be on the order of 97% below and 20% above the 4.5-μ region. In view of the fact that the spacecraft OSR

SPACECRAFT

LIQUID NITROGEN

SECOND-SURFACE
MIRROR REFLECTORS

TUNGSTEN
LAMP BANK
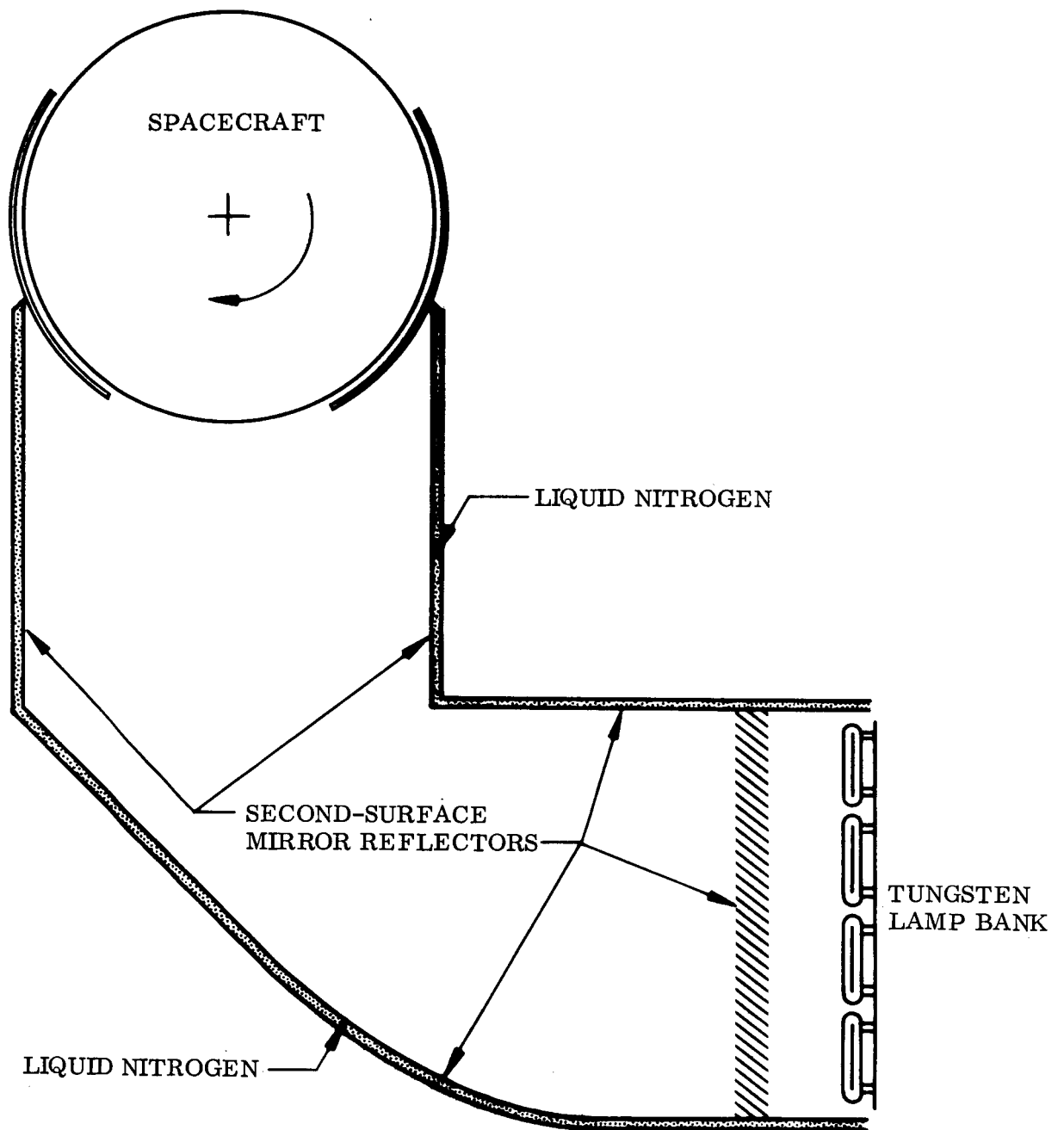
LIQUID NITROGEN

Figure 17   Energy Source and Spacecraft Arrangement Using
Liquid-Nitrogen-Cooled, Second-Surface Mirror
Reflectors

surfaces have roughly these same properties for tungsten irradiation, it is necessary that a minimum of three bounces occur for all rays leaving the lamp bank prior to impingement on the satellite surface. This estimate is based upon the energy distributions observed on the lamp bank used in this program for model irradiation.

For the model-test lamp bank, it was found that, at full voltage (115 V), the percentage of energy beyond 4.5 μ was 38%. For direct irradiation of the model's OSR surfaces, this resulted in an α/ϵ to the simulated flux of 0.43 instead of the space value of 0.10. For the second surface reflector system, shown in Figure 17, the effective α/ϵ of the OSR surfaces irradiated by the source would be modified according to the amount of infrared energy absorbed by the mirrors. For energy undergoing a single reflection, the α/ϵ would be 0.204, 0.124 for two reflections, and 0.105 for three reflections. These results are based on the assumption that all reflecting surfaces are maintained at liquid nitrogen temperatures. They provide evidence that at least three reflections should occur for all rays in order to eliminate the required amount of unwanted infrared energy.

This reflector system could be designed for illumination of the entire cylindrical section of the satellite. However, the approach would require a separate source system for heating of the despun antenna. It does not appear feasible to design a single tungsten system that would allow simultaneous illumination of the body and antenna and at the same time provide no direct irradiation for the top cover. The analytical model constructed for the prototype provided results which indicate that the antenna is sufficiently decoupled thermally from the main body so that its thermal performance has little influence on internal temperatures. Under this condition, it is possible to provide a separate source for irradiation of the antenna and to utilize absorbed flux or prescribed temperatures for control of this source.

The absorbing surfaces used to eliminate infrared energy from the source system will result in a loss of efficiency for transmission of useful energy from the source to the test surface. The overall efficiency of the system shown in Figure 17 is not known since an exact determination would require an experimental evaluation. However, the lamp power required for the spacecraft tests has been estimated on the basis of the performance of the lamp array used on the half-scale thermal model. This power is given in Table 18 which also indicates estimates of the power requirements for other approaches. The computation of power assumed that all energy from the lamp bank struck three absorbing surfaces before arrival at the test plane. Therefore, the result obtained is likely to be less than the actual requirements since more than three reflections will occur for certain portions of the energy. Other losses will also occur that cannot be evaluated without consideration of a detailed design.

The second potential filtering technique provides short wavelength tungsten energy at the test plane through the use of water-cooled envelopes surrounding each lamp. The location of the tungsten lamp bank with respect to the spacecraft would be similar to that used for the half-scale model tests (Figure 12). Liquid-nitrogen-cooled, polished-aluminum shields would be employed to direct the maximum amount

TABLE 18. – ESTIMATE OF POWER REQUIRED TO PLACE 25 SOLAR CONSTANTS ON SPACECRAFT USING TUNGSTEN ENERGY

Potential testing technique	Power[a] (kW)
Second-surface[b] mirror reflectors	110
Water-cooled[c] lamp enclosures	220
Zonal heating[d]	35

[a] Power includes that required to irradiate antenna.
[b] Computed on the basis of 3 reflections for all energy striking the vehicle. Results in an α for solar cells of 0.53, α for OSR of 0.024.
[c] Computed on basis of G.E. T3-500 tungsten lamp spectrum at wavelengths less than 1.4 μ. Assumes 85% transmission through water filter. Results in an α for solar cells of 0.64, α for OSR of 0.012.
[d] Absorbed heat flux simulation using unfiltered tungsten lamps. Assumes α for upper solar array of 0.55, α for viewing band of 0.34, α for lower solar array of 0.80, α for lower array heat shield of 0.34.

of energy toward the test plane. Presently available data indicate that water-cooled enclosures around the tungsten lamps would absorb all energy beyond 1.4 μ. This results in an α for the remaining tungsten energy of 0.012 for the silver-coated fused silica OSR and 0.64 for the filtered silicon solar cells. Such deviations from the actual solar absorptance values would result in an undesirable distribution of absorbed energy. Other potential problems which arise when using this technique include long wavelength energy emission from the water-cooled envelopes and extremely high input power requirements (Table 18) to operate the tungsten lamp bank system. Preliminary calculations indicate that the absorption of infrared energy on the viewing band due to emission from the water enclosures could be as high as 40 W. Only 18 W is absorbed by the same region due to solar irradiation at the 1-sun level. At 25 solar constants, 40 W represents an increase in absorbed energy for the viewing band of approximately 9%.

The third potential testing technique consists of absorbed heat flux simulation through zonal heating of the cylindrical section. The tungsten source and shielding systems required could be arranged as shown in Figure 18. Three separately controlled tungsten lamp bank systems provide required absorbed heat flux for each

TUNGSTEN
LAMP BANK

TUNGSTEN
LAMP BANK

REFLECTIVE SHIELDS
- LN$_2$ COOLED
- POLISHED ALUMINUM
  INNER SURFACES
- BLACK PAINT ON
  EXTERIOR SURFACES
- SUSPENDED FROM
  STRUCTURE IN
  TEST CHAMBER

TUNGSTEN
LAMP BANK
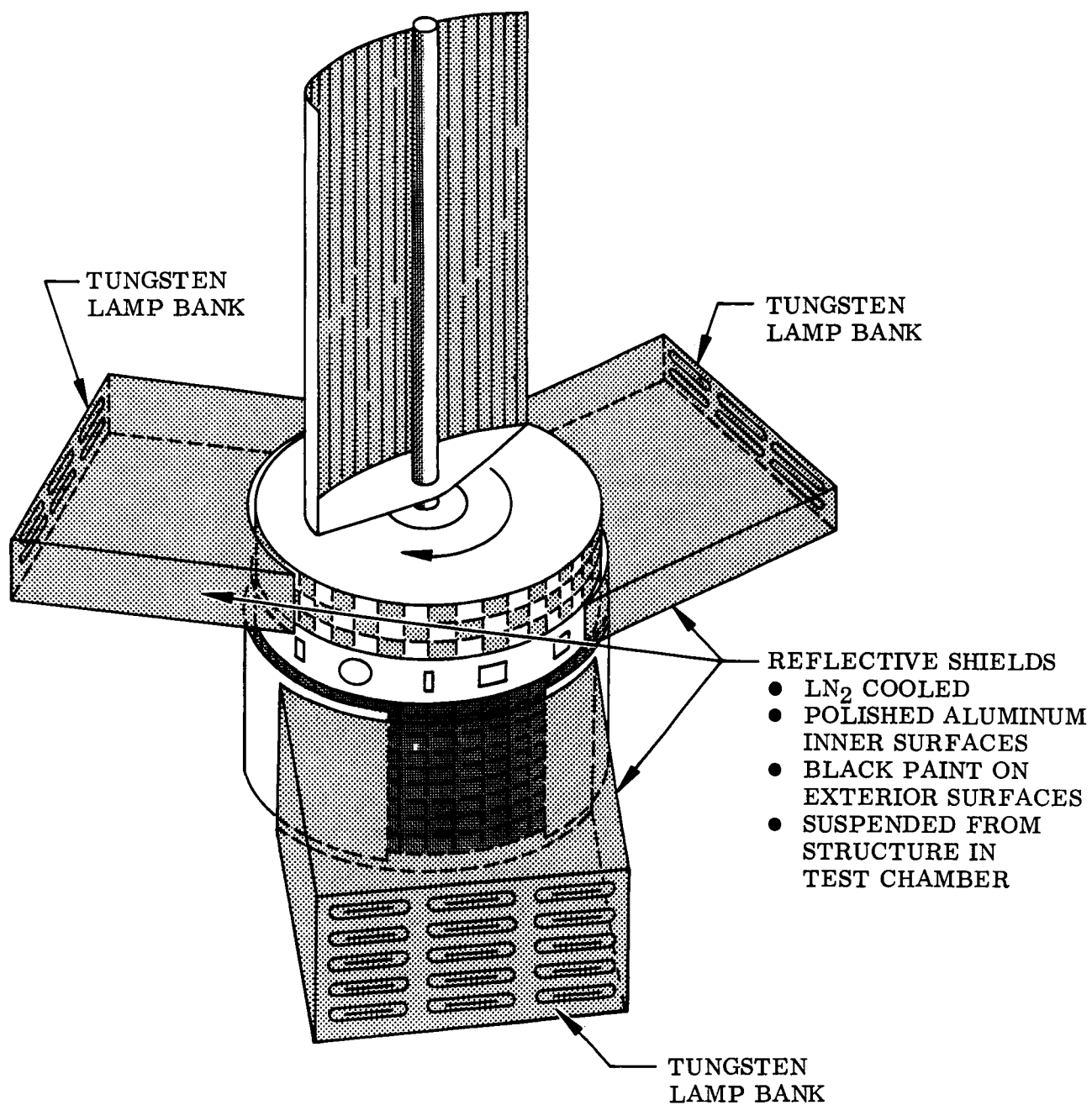
Figure 18   Energy Source and Shielding Arrangement for Controlled
Absorbed Heat Flux Simulation

separate section of the vehicle. The approach requires accurate knowledge of surface properties in combination with a precise definition of the source spectral radiance characteristics. The lamp bank shields employed are liquid nitrogen cooled and polished on the interior surfaces. An additional source is needed for irradiation of the antenna where either prescribed temperatures or heat fluxes are the basis for control of the bank. The source input power requirement for this technique, as shown in Table 18, is less than that required for the previously described systems. This is due to the high infrared absorptances of the spacecraft surfaces and maximum utilization of energy emitted by the lamps.

The experiment booms used on the advanced Pioneer spacecraft introduce additional difficulties when using any of the previously described simulation approaches. When using the first technique, it is impractical to provide energy from a carbon arc or filtered xenon arc over the entire volume occupied by the booms. For the tungsten sources, the required reflective shields interfere with the rotational path swept by the booms. Furthermore, inclusion of the booms during testing leads to the need for a considerably larger space chamber than that required for all other components of the spacecraft. Therefore, it is recommended that the actual booms be removed during thermal performance testing and that their thermal influence be simulated by indirect means.

The thermal analyzer computer program used to predict prototype performance indicated that the booms account for only a small portion of the energy entering or leaving the instrument platform. The results also showed that the booms are nearly isothermal over the majority of their length. These characteristics permit the substitution of short stubby booms whose temperatures would be separately controlled. It is obvious that additional analytical work must be accomplished to establish the design of these simulated appendages.

Each of the potential testing techniques described assumes that the spacecraft is spinning within the simulation chamber and that good thermal isolation is provided between the spacecraft and required supporting structure. Each technique requires appropriate shielding of the tungsten lamp system to provide maximum power at the test plane and to prevent energy from impinging on areas of the vehicle not normally exposed to solar irradiation in space.

The shielding, absorbing, and filtering techniques suggested for the tungsten sources require further investigation to establish optimum conditions. The efficiency, spectral distribution, and total power requirements stated throughout this section have been estimated on the basis of the measurements made with the half-scale model. The lamps used were G.E. T3-500 W, wound filament, quartz enclosed, high temperature lamps. These units run at lower filament temperatures than the newer iodide-doped lamps and, for this reason, are not as efficient for generation of short wavelength energy. Unfortunately, the increase in short wavelength spectral emissive power that could be gained by use of higher filament temperatures cannot be stated since confirming measurements were not made. However, available evidence indicates that some improvement can be obtained by the higher filament temperatures. On the basis of

spectral power measurements made previously by this laboratory, it is known that at full voltage the iodide-doped lamps have an effective filament temperature near 3200° K. The maximum filament temperature at rated voltage of nondoped lamps is close to 2400° K. Therefore, 97% of the energy emitted by the high-temperature tungsten filament is at wavelengths shorter than 4.5 μ, as compared to 93% for the low-temperature filament. This shift to shorter wavelengths is an advantage. However, the shorter filament used at a higher watt density will result in higher temperatures for the quartz enclosure which then emits undesirable infrared energy toward the specimen. Of course the smaller size of the envelope results in less cold wall blockage. The overall effect of these characteristics must necessarily be determined experimentally on an assembled lamp bank.

In conclusion, the techniques suggested for testing of the prototype spacecraft each have definite advantages and limitations in terms of the spacecraft surface properties and geometry. Carbon arc and filtered xenon arc solar simulators are optimum for simulation of the solar spectrum during testing of the spacecraft and would result in a thermal response that closely matched actual flight conditions. The unavailability of such units having a capability of 25 solar constants as well as their probable excessive cost are serious drawbacks.

The tungsten sources are considerably more economical than high intensity arc simulators but these systems require significant alteration of their spectral distribution to obtain the proper distribution of absorbed energy. Table 18 shows the power requirements for several tungsten lamp approaches wherein a total of 25 solar constants is placed on the vehicle. The values of α (footnoted in the table for the modified spectral emissive powers), clearly show that the distribution of absorbed energy will not be the same with the tungsten sources as that anticipated for the extraterrestrial sun. The thermal response of the prototype to these changes in surface absorptance was not determined during this program. Such determinations remain to be made as part of a continuing and detailed evaluation of the suggested techniques. However, sufficient evidence has been accumulated during the program to permit the conclusion that the use of tungsten energy is a feasible approach given that procedures are instituted to filter out or absorb the undesirable content of infrared energy. In lieu of such procedures, it is possible to provide zonal heating on the basis of absorbed flux. More consideration should be given to the advantages and limitations of using this approach, in combination with a more highly refined thermal analyses of the actual hardware.

None of the techniques considered during this study will permit testing of the actual spacecraft experiment booms during the performance evaluations. It is recommended that the actual booms be removed and shorter, simulated appendages whose temperatures can be separately controlled, be installed in their places.

Section 9

CONCLUSIONS AND RECOMMENDATIONS

The results obtained from the analytical and experimental models used during this program showed that thermal performance testing of the advanced Pioneer spacecraft cannot be accomplished by <u>direct</u> illumination from unfiltered quartz-enclosed tungsten filament lamps. The infrared energy emitted by the tungsten lamps beyond 4.5 μ resulted in greatly increased energy absorption by the OSR (optical solar reflector second-surface mirrors) surfaces on the half-scale model. This caused a totally unsatisfactory distribution of absorbed energy into the major surface zones. However, analyses of the results obtained indicated that acceptable absorptances could be achieved using tungsten sources, provided that energy beyond 4.5 μ is eliminated. Other forms of solar simulation such as carbon arc or filtered xenon arc would provide satisfactory results for the prototype spacecraft; however, such units are presently unable to provide the required high-energy flux (25 solar constants) over the entire test plane. The development of a solar simulator with a 25-sun intensity capability is technically feasible; however, such an endeavor is economically undesirable.

The analytical and experimental results obtained for the half-scale model led to the conclusion that similar problems would occur during thermal performance testing of the actual spacecraft if tungsten lamps were employed without consideration of their infrared energy emission beyond 4.5 μ. In addition to increased energy absorption by the OSR-covered surfaces, the solar cells with their nongray spectral reflectance characteristics would also contribute to an improper distribution of absorbed energy on the spacecraft surfaces.

Despite the difficulties involved with the use of tungsten filament lamps, sufficient evidence was accumulated during this program to conclude that the use of tungsten energy is a feasible method of providing the required heat flux for thermal testing of the spacecraft. To employ this method, however, will require implementation of one of the following approaches:

- Filtering of the tungsten lamp energy to eliminate the unwanted infrared portion

- Zonal heating with unfiltered tungsten energy to provide controlled absorbed heat flux simulation

Preliminary studies indicate that the first approach could be accomplished by placing liquid-nitrogen-cooled, second-surface mirror reflectors between the source and the spacecraft. This technique would essentially eliminate from the test plane all of the energy beyond 4.5 μ. Another filtering technique that should be considered

is to surround each lamp with a water-cooled enclosure, thereby trapping all energy emitted from the source beyond 1.4 μ. The second approach, consisting of absorbed heat flux simulation, would use three separately controlled tungsten lamp-bank systems to provide the required heat flux to the major zones of the spacecraft. Each of these approaches has definite advantages and limitations in terms of the spacecraft surface properties and geometry. However, further investigation is required to determine which approach provides the optimum conditions for testing of the prototype.

The half-scale model was designed in accordance with accepted thermal modeling laws and included the major nodes and connecting thermal resistances of the prototype spacecraft. It was not designed to provide a precise thermal match of the spacecraft; however, its sensitivity to external energy sources was sufficiently similar to that of the prototype to provide much needed information on spacecraft performance under space simulated conditions. The difficulties experienced during construction, analyses, and testing of the model provided some indication of potential problem areas with respect to conducting a similar program on the prototype spacecraft. Those areas suggested for further study during development of the prototype hardware are: (1) more exact definition of the thermal properties of the multilayer insulation systems; (2) better techniques for attaching the OSR and the multilayer insulation blankets; and (3) establishment of a more detailed thermal analyzer computer model that would include more exact definition of the thermal conduction and radiation heat-flow paths as well as an improved representation of the temperature dependence of the multilayer insulation.

The thermal analyzer computer model provided a means of predicting the space performance of the model and thereby provided a basis for evaluation of test results. Predictions were made for 1 sun of solar energy and for 1, 5, and 9 solar constants of tungsten energy. In general, the computed results compared favorably with test results. At the high flux levels, however, temperature correlation for some areas of the vehicle was poor. The poor comparisons were apparently due to the use of a minimum number of nodes for the analyzer model and its insensitivity to the thermally induced property changes of the multilayer insulation.

Further refinements of the thermal analyzer model to include exact definition of multilayer insulation properties and radiative heat-flow paths would lead to an improvement of the accuracy of the computed results. In its present form, the analysis was sufficiently sensitive to the external boundary conditions used on the model to adequately demonstrate the gross thermal errors caused by the use of unfiltered tungsten lamps. Further work using the half-scale test model would be considerably enhanced by a revision of the existing computer program so that more precise comparisons could be obtained.

It is recommended that further work be performed to investigate in detail each of the previously proposed testing techniques so that their applicability to the prototype spacecraft can be verified. It is recommended that the available half-scale thermal model be utilized in all such future work so that actual experience can serve as a major source of information in specification of the hardware test program. It is

also recommended that the present thermal analyzer computer model of the half-scale test model be refined where necessary so that a better understanding of test results can be established. The additional effort would lead to a more complete definition of required test procedures than was possible within the scope and level of effort provided for the present program.

Section 10

REFERENCES

1. Matthews, H. F.; and Erickson, M. D.: The NASA Advanced Pioneer Mission. NASA TMX-54, 039, presented at the National SAE-ASME Meeting, New York, April 1964.

2. Anderson, J. W.; La Blanc, E. A.; and Cohan, H.: Experimental and Analytical Assessment of Space Thermal and Vacuum Environment Simulation Requirements, J. Spacecraft, vol. 3, no. 7, July 1966.

3. Anderson, J. W.; La Blanc, E. A.; and McNally, M.: Space Thermal Simulation Without a Solar Simulator. Proceedings of International Symposium on Solar Radiation Simulation. Los Angeles, Calif., Jan 18−20, 1965.

4. Latture, N. C.: Experimental Correlation Between Heat Flux and Solar Irradiated Surfaces. Proceedings of International Symposium on Solar Radiation Simulation, Los Angeles, Calif., Jan 18−20, 1965.

5. Rolling, R. E. et al.: Development of Thermal-Vacuum Testing Techniques for Spacecraft at High Solar Intensities. NASA CR 73066, Dec 1966.

6. Marshall, K. N.; and Olson, R. L.: Optical Solar Reflector Thermal Control Surface. LMSC 3-56-65-2 [Air Force Contract AF-04(647)-787], Lockheed Missiles & Space Company, Palo Alto, Calif., Feb 1965.

7. Greenburg, S. A.; and Vance, D. A.: Low Solar Absorptance and Emittance Surfaces Utilizing Vacuum Deposited Techniques. NASA CR 73039, 1966.

8. Streed, E. R.; Cunnington, G. R.; and Zierman, C. A.: Performance of Multilayer Insulation Systems for the 300°K to 800°K Temperature Range. Thermophysics and Temperature Control of Spacecraft and Entry Vehicles, Progress in Astronautics and Aeronautics, vol. 18, Academic Press, 1966, pp. 735−772.

9. Cunnington, G. R.; Zierman, C. A.; Funai, A. I.; and Lindahn, A.: Performance of Multilayer Insulation Systems for Temperatures to 700°K. Final Report on Contract NAS 2-2441, May 1967.

10. Rolling, R. E.: Results of Transient Thermal Modeling in a Simulated Space Environment. Thermophysics and Temperature Control of Spacecraft and Entry Vehicles, vol. 18, Academic Press, 1966, pp. 627−659.

11. Katzoff, S.: Similitude in Thermal Models of Spacecraft. NASA TND-1631, 1963.

12. Thermal Analyzer Control System for IBM 709-7090-7094 Computer Engineering Utilization Manual. LMSC 3-56-65-8, Lockheed Missiles & Space Company, Sunnyvale, Calif., Sep 1965.

Appendix A
PHASE I THERMAL ANALYZER COMPUTER PROGRAM

A.1 GENERAL DESCRIPTION OF THERMAL ANALYSES

The thermal analyzer computer model was established during Phase I of the program both for prediction of anticipated flight temperatures and for prediction of temperatures under simulated space conditions. Computer models of both the solar powered (Figure 1) and the RTG-powered (Figure 19) configurations were constructed for predicting the temperature response for vehicle-sun distances of 1.0 and 0.2 AU. These models comprised 43 and 45 nodes, respectively. The nodes were connected by thermal conduction and radiation resistances calculated or approximated from available advanced Pioneer spacecraft description, and supplemented by design changes proposed by NASA Ames personnel. The analyzer models were constructed for solution by LMSC's Mark-5C Thermal Analyzer Computer Program (ref. 12).

For the thermal analyses, the spacecraft was assumed to be moving in an elliptical orbit about the sun with perihelion at 0.2 AU and aphelion at 1.0 AU. The orbit was assumed to be in the plane of the ecliptic, and the spacecraft was assumed to be spin-stabilized at 60 rpm with the axis of spin normal to the plane of the ecliptic. The spectral distribution of solar energy (Figure 4) was assumed to be the same for both 0.2 and 1.0 AU; the sun was assumed to be a point source; and incident solar energy at 0.2 AU was taken to be 25 times that at 1.0 AU (i.e., 3.5 W/cm^2). Albedo and earth emission were neglected for the 1.0 AU case. During this analysis, the upper solar cell array was assumed to be entirely covered with solar cells, while the other surfaces were coated as described previously in this report. Important assumptions in assigning node locations and determining thermal resistances were as follows:

- Circumferential variations in temperature around the spacecraft due to its finite spin rate were considered negligible. (This assumption was based on vehicle symmetry and results of quasi-steady state calculations described in ref. 5.)

- Equipment was considered symmetrically located on the platform, thus allowing the majority of equipment to be combined into one node. Experiments directly exposed to the external environment were separated according to their window surface characteristics.

- The louver system was assumed to operate uniformly under all sections of the equipment platform, and temperature gradients through the louvers were considered negligible.

132

152

122

91.5

20.3

16.5

36.8

25.4
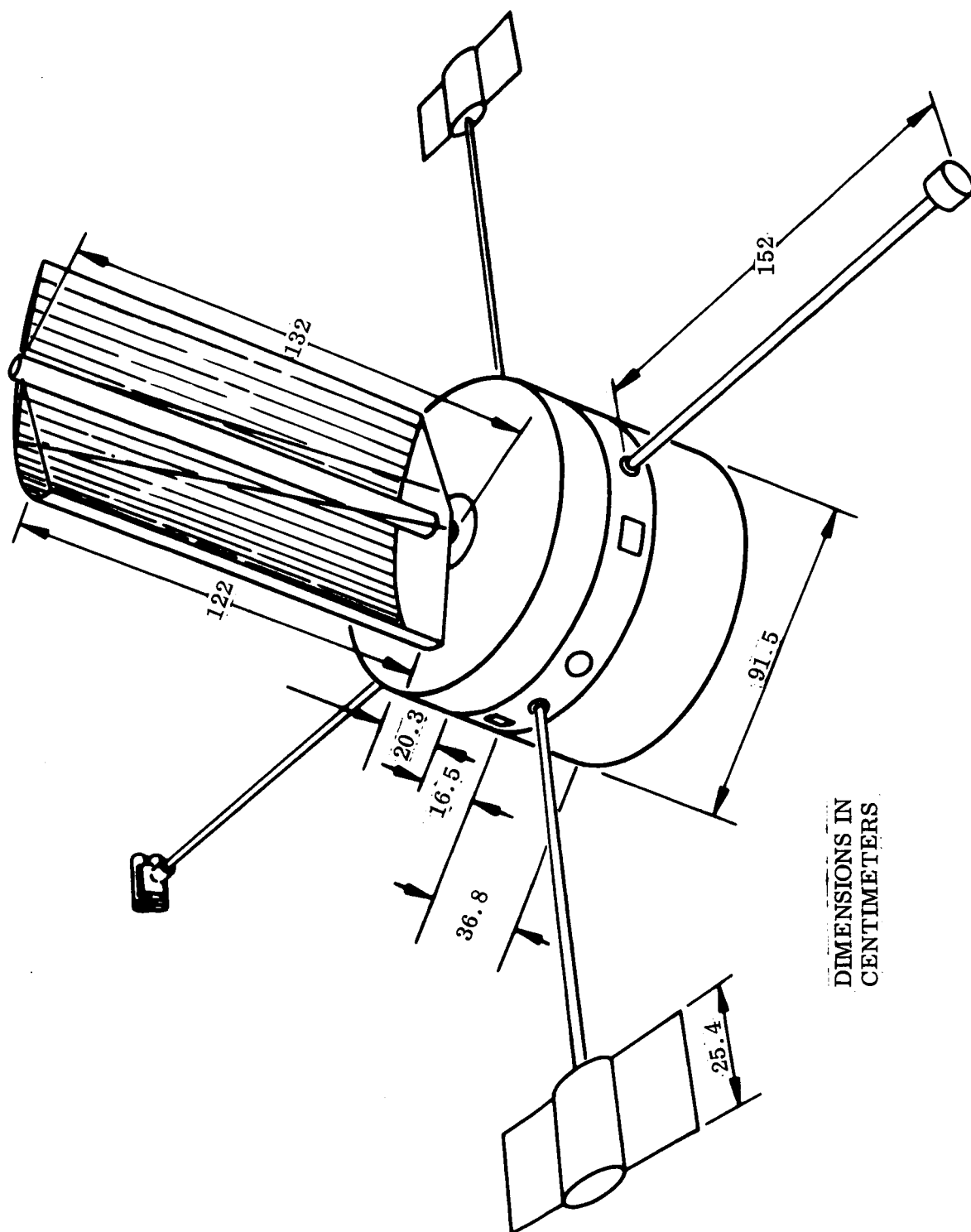
DIMENSIONS IN
CENTIMETERS

Figure 19 Spacecraft RTG–Powered Configuration

- Louver system operation was approximated by varying the emittance of the underside of the equipment platform linearly with the platform's temperature.

- Solar heat rates into all exposed surfaces were approximated by taking the average over one complete vehicle revolution.

- Internal power dissipation was assumed constant at 50 W.

- An effective thermal conductivity of 8.6×10^{-6} W/cm^2 °K was used for all multilayer insulation blankets.

- Changes in surface optical properties with prolonged space environmental exposures were neglected.

- Variations in material properties with changes in temperature were neglected.

Assumptions pertaining to solar-powered configuration only:

- The variable aperture heat shield surrounding the lower array was considered conductively insulated from the spacecraft, and its inner surface was assumed in thermal equilibrium with the lower array.

- The three experiment booms were combined into one boom by multiplying the thermal resistance of one boom by one-third.

Assumptions pertaining to RTG-powered configuration only:

- The solar arrays were replaced with the OSR thermal control surface.

- The lower array section was shortened by 19.7 cm.

- The four booms (two RTG booms and two experiment booms) were simulated by two equivalent booms, each having twice the actual input energy flux and half the actual boom thermal resistance.

A.2 COMPUTER MODEL DESCRIPTION

Thermal analyzer node locations for both the solar-powered and RTG-powered configurations are shown in Figure 20. Descriptions of the various nodes are provided in Table 19.

The thermal model for the solar-powered configuration was developed with the following characteristics:

- 43 nodes

- 55 conduction resistors

64

Node 1 is outer space.

*Node peculiar to solar-powered configuration.
**Node peculiar to RTG-powered configuration.
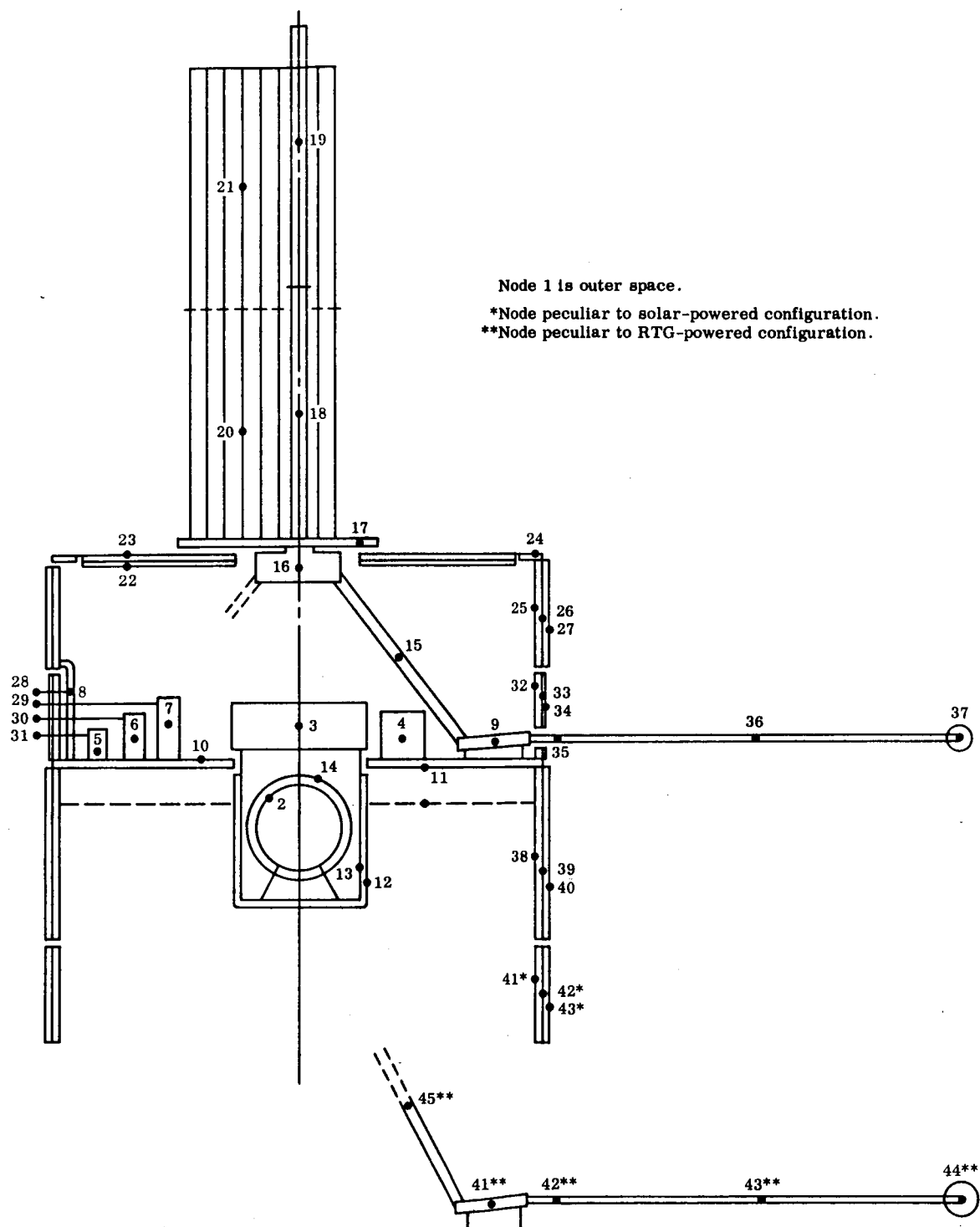
Figure 20 Thermal Analyzer Model Node Locations

65

TABLE 19. – THERMAL ANALYZER MODEL NODE LIST

Node	Description
1	Space
2	Gas bottle
3	DTU equipment package
4	Average equipment package
5	MIT experiment
6	Ames experiment
7	Chicago and GRCSW experiment
8	Sun sensors
9	Antenna support and experiment boom bracket
10	Upper platform
11	Lower platform and louvers
12	Cylinder insulation surface
13	Cylinder inner surface
14	Gas bottle insulation surface
15	Antenna base supports
16	Antenna base and motor
17	Antenna platform
18	Antenna dipole, lower
19	Antenna dipole, upper
20	Antenna reflector, lower
21	Antenna reflector, upper
22	Top cover, inside
23	Top cover, outside
24	Upper frame
25	Upper array, insulation surface
26	Upper array, insulation middle
27	Upper array, outside
28	Sun sensor, outside

Node	Description
29	Chicago and GRCSW experiment, outside
30	Ames experiment, outside
31	MIT experiment, outside
32	Viewing band insulation, inner surface
33	Viewing band insulation, middle
34	Viewing band insulation, outer surface
35	Experiment boom, base
36	Experiment boom, middle
37	Experiment boom, end
38	Lower array, forward, insulation surface
39	Lower array, forward, insulation middle
40	Lower array, forward, outside

Solar powered only

Node	Description
41	Lower array, aft, insulation surface
42	Lower array, aft, insulation middle
43	Lower array, aft, outside

RTG powered only

Node	Description
41	RTG boom bracket
42	RTG boom, base
43	RTG boom, middle
44	RTG boom, end including RTG
45	Antenna base supports, RTG

66

- 64 radiation resistors
    - 24 radiation-to-space resistors
    - 40 component-to-component radiation resistors
    - 4 radiation constants associated with the lower instrument platform and louver surface

- 21 heat rates introduced into the analog network
    - 5 constant internal heat rates
    - 16 variable external heat rates corresponding to solar distance

The thermal model for the RTG-powered configuration was developed with the following characteristics:

- 45 nodes

- 56 conduction resistors

- 70 radiation resistors
    - 25 radiation-to-space resistors
    - 45 component-to-component radiation resistors
    - 3 radiation constants associated with the lower instrument platform and louver surface

- 24 heat rates introduced into the analog network
    - 6 constant internal heat rates
    - 18 variable external heat rates corresponding to solar distance

A.3 HEAT RATE COMPUTATION

Solar heat rates for continuously illuminated surfaces at 1 AU were calculated using the relation

$$Q(W) = \alpha_s A_p (cm^2) \; 0.14 \left(\frac{W}{cm^2} \right) \tag{A.1}$$

For plane, or nearly plane, surfaces rotating at a constant rate with respect to the vehicle-sun line, solar heat rates at 1 AU were found using the relation

$$Q(W) = \alpha_s \frac{A}{\pi} (cm^2) \; 0.14 \left(\frac{W}{cm^2} \right) \tag{A.2}$$

67

Solar heat rates for 0.2 AU were calculated by multiplying the heat rates found at 1 AU by $(1/0.2)^2 = 25$. Determination of solar heat rates into the lower solar cell array was unnecessary for the solar-powered configuration at 0.2 AU, since the despun shield controls the array temperature to a maximum value of 366°K. The 0.2-AU heat rates into the experiment apertures were reduced to the 1-AU level because of the variable shutter system to be employed.

Solar heat rates for the solar-powered and RTG-powered configurations are given in Tables 20 and 21, respectively.

Power dissipation from sources internal to the vehicle is given in Table 22. The equipment shown is common to both vehicle configurations analyzed, with the exception of the two RTG power units (node 44) which apply only to the RTG-powered configuration.

A.4 ENERGY EXCHANGE BY CONDUCTION

One-dimensional conduction resistance between the various nodes was either estimated using best engineering judgment where details of vehicle configuration were unavailable or calculated where possible using the relation

$$R_{ij} \left(\frac{°K}{W}\right) = \frac{L(cm)}{k\left(\frac{W}{cm\ °K}\right) A(cm^2)} \tag{A.3}$$

In cases where conductive resistances were found to be less than 5.27×10^{-2} °K/W, a value of 5.27×10^{-2} °K/W was used in the computer calculation. Excessive computer calculation time is avoided by using a value such as this for conduction resistance, and experience has shown that no significant error results in the final equilibrium temperatures.

A relation for heat conduction parallel to the facing sheets in the honeycomb structure was developed from honeycomb geometry. For 0.635 cm, aluminum honeycomb with 0.0254 cm thick fiberglass facing sheets, the following relation for conduction resistance was used:

$$R_{ij} \left(\frac{°K}{W}\right) = \frac{L_1}{L_2} (392) \left(\frac{°K}{W}\right) \tag{A.4}$$

where L_1 and L_2 are as shown in Figure 21.

TABLE 20. – SOLAR HEAT RATES TO EXTERNAL SURFACES AT 1 AU, SOLAR-POWERED CONFIGURATION

Description	Node	Projected area, A_p (cm²)	α_s	Heat rate relation used	Heat rate (W)	Comments
Dipole antenna and reflector	17	154.8	0.08	A-1	1.74	OSR surfaces degraded from α_s = 0.04 to 0.08 due to curvature of surfaces
	18	335.5	.08	A-1	3.76	
	19	335.5	.08	A-1	3.76	
	20	980.7	.25	A-1	34.3	White paint on reflector section of antenna
	21	980.7	.25	A-1	34.3	
Solar-cell arrays	27	1922.7	.69	A-1	186	
	40	3367.9	.69	A-1	325	
	43	1806.6	.69	A-1	174	
Viewing band	34	1342.0	.04	A-1	7.51	
Booms	35	261.3	.08	A-2	0.928	Three booms combined and divided into three radial lengths with OSR surfaces degraded from α_s = 0.04 to 0.08 due to curvature of surfaces
	36	519.4	.08	A-2	0.622	
	37	774.2	.08	A-2	0.186	
Five sun sensors	28	133.9[a]	.4	A-2	2.38	White paint with holes
Experiments No. 4 and No. 6	29	72.3[a]	.1	A-2	0.322	OSR with holes
Experiment No. 7	30	4.19[a]	1.0	A-2	0.185	Opening assumed to be blackbody
Experiment No. 2	31	91.0[a]	.5	A-2	2.025	Aluminum with holes

[a]Total area (A).

TABLE 21. – SOLAR HEAT RATES TO EXTERNAL SURFACES AT 1 AU, RTG-POWERED CONFIGURATION

Description	Node	Projected area, A_p (cm²)	α_s	Heat rate relation used	Heat rate (W)	Comments
Dipole antenna and reflector	17	154.8	0.08	A-1	1.74	OSR surfaces degraded from α_s = 0.04 to 0.08 due to curvature of surface
	18	335.5	.08	A-1	3.76	
	19	335.5	.08	A-1	3.76	
	20	980.7	.25	A-1	34.3	White paint on reflector section of antenna
	21	980.7	.25	A-1	34.3	
OSR arrays	27	1922.7	.04	A-1	10.8	
	40	3367.9	.04	A-1	18.9	
Viewing band	34	1342.0	.04	A-1	7.51	
Two booms	35	55.5	.08	A-2	0.622	Two booms combined and divided into three radial lengths with OSR surfaces assumed degraded from α_s = 0.04 to 0.08 because of surface curvature
	36	111.0	.08		1.24	
	37	161.0	.08		1.80	
RTG booms	42	55.5	.08	A-2	0.622	The booms combined and divided into three radial lengths with OSR surfaces assumed degraded from α_s = 0.04 to 0.08 because of surface curvature
	43	111.0	.08		1.24	
	44	516.0	.08		5.78	
Five sun sensors	28	133.9[a]	.4	A-2	2.38	White paint plus holes
Experiments No. 4 and No. 6	29	72.3[a]	.1	A-2	0.322	OSR plus holes
Experiment No. 7	30	4.19[a]	1.0	A-2	0.185	Opening assumed to be blackbody
Experiment No. 2	31	91.0[a]	.5	A-2	2.03	Aluminum plus holes

[a]Total area (A).

TABLE 22. – HEAT SOURCES INTERNAL TO VEHICLE

Equipment	Node	Power (W)
DTU box located over gas bottle	3	1.0
All other equipment on platform	4	46.0
Experiment no. 2	5	0.5
Experiment no. 7	6	1.0
Experiments no. 4 and 6	7	2.6
Two RTG Units[a]	44	1200

[a]Pertains to RTG-powered configuration only.
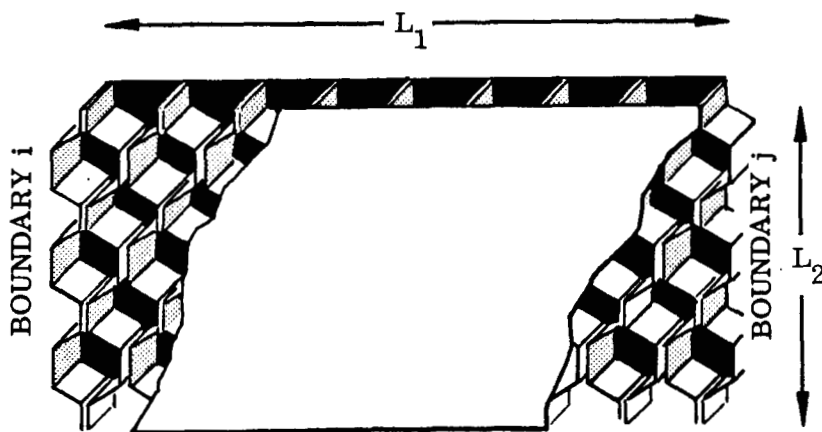
Figure 21 Honeycomb Schematic

71

Conduction resistances and specific assumptions used in their determination are given in Table 23 for both the solar-powered and RTG-powered configurations. Resistances peculiar to each configuration are noted.

A.5 ENERGY EXCHANGE BY RADIATION

Radiant energy exchange between the various nodes was calculated by a finite-difference electrical analog method which uses a linearized radiation resistance defined by

$$R_{ij}\left(\frac{°K}{W}\right) = \frac{1}{(RADK_{ij}) \, \sigma \left(T_i^2 + T_j^2\right) (T_i + T_j)}$$

where

$$RADK_{ij} \equiv \frac{A_i Fa_{ij} Fe_{ij}}{3600} \left(\frac{cm^2\text{-}hr}{sec}\right)$$

$$Fe_{ij} \doteq \epsilon_i \epsilon_j$$

All radiant exchange factors, $RADK_{ij}$, can be calculated in a straightforward manner using the above relations except the following:

(1) Radiation between the louver system, with its variable effective emittance imaginary surface, and all surfaces which "see" the louver system

(2) The lower solar cell array, which has only half of its surface area exposed to space

The louver system effective emittance is a linear function of lower platform temperature as plotted in Figure 22.

Radiation exchange factors, $RADK_{ij}$, and specific assumptions used in their determination are given in Table 24 for both the solar-powered and RTG-powered configurations. Radiation exchange factors that are peculiar to each configuration are noted.

A.6 RESULTS

Results from the computer analysis are presented in Figures 23 and 24 where individual node temperatures for the 1.0 and 0.2 AU conditions are shown. In addition, the analysis considered variations in the major heat-flow paths and variations in performance of the multilayer insulation system. These were considered with respect to their effects on temperature performance of the instrument platform. Complete details of these results and results of other studies performed during Phase I may be found in ref. 5.

TABLE 23. – THERMAL CONDUCTION RESISTANCES

Resistor no.	Node description	Connecting nodes i–j	Resistance value °K/W	Assumptions
1	Antenna dipole	19–18	9.955	$L = 66.04$ cm
2	Antenna dipole to motor	18–16	4.977	$L = 33.02$ cm — Al tubing, 5.08 cm O.D., 0.254 cm thick, $k = 1.731$ W/cm °K
3	Antenna reflector	21–20	5.267	$L = 58.42$ cm
4	Antenna reflector to antenna platform	20–17	2.686	$L = 29.2$ cm — 55 Al tubes, 0.318 cm O.D., $A_x = 0.116$ cm²/tube, $k = 1.731$ W/cm °K
5	Antenna platform bearing	17–16	52.67	Estimated resistance across bearing and drive.
33[a]	Antenna motor to	16–15	43.87	Stainless steel tubing, $L = 17.78$ cm, $A_x = 0.77$ cm²/tube, $k = 0.173$ W/cm °K. Contact resistance assumed to be 4.74 °K/W. Total resistance of one support $= R_1 = 1.32 \times 10^2$. Three supports are combined into one resistance by dividing R_1 by 3.
34[a]	boom brackets	15–9	43.87	
37[a]	Boom to boom brackets	35–9	0.1754	Contact resistance assumed.
36[a]	Boom	36–35	4.609	Al tubing, $L = 76.20$ cm, 2.54 cm O.D., $A_x = 3.187$ cm²/tube, $k = 1.731$. Three booms combined.
35[a]	Boom	37–36	4.609	
38[a]	Boom brackets to instrument platform	9–10	18.22	Contact resistance assumed
31	Outside to exp. no. 2	31–5	0.0527	Resistance actually < 5.27×10^{-2}
29	Outside to exp. no. 7	30–6		
27	Outside to exps. no. 4 & 6	29–7		
25	Outside to sun sensor	28–8		
40	DTU package to platform	3–10		
39	All other equipment	4–10		
32	Experiment no. 2	5–10		
30	Experiment no. 7	6–10		
28	Experiments no. 4 & 6	7–10		
26	Sun sensor bracket	10–8		
41	Through instrument platform	10–11		
42	Platform to cylinder	11–13	0.5267	Magnesium, $L = 11.43$ cm, $A_x = 5.065$ cm², $k = 1.212$
43	Cylinder to gas bottle	13–2	437.2	Teflon, $L = 3.81$ cm, $A_x = 5.065$ cm², $k = 0.173 \times 10^{-2}$
24	Sun sensor bracket to upper solar array	27–8	26.34	High resistance required to isolate array at 0.2 AU orbit.

Insulation resistance perpendicular to layers:

Resistor no.	Node description	Connecting nodes i–j	Resistance value °K/W	Assumptions
8	Top cover	23–22	22.75	$L = 1.27$ cm, $A_x = 6500$ cm², multilayer $k = 8.66 \times 10^{-6}$
14	Top array	25–26	18.86	$L = 0.953$ cm, $A_x = \pi(91.44 \times 20.32)$ cm² — multilayer $k = 8.66 \times 10^{-6}$
15		26–27	6.268	$L = 0.318$ cm, $A_x = \pi(91.44 \times 20.32)$ cm²
19	Viewing band	32–33	11.110	$L = 0.953$ cm, $A_x = \pi(91.44 \times 17.15)$ cm² — Degraded multilayer $k = 1.731 \times 10^{-5}$
20		33–34	3.740	$L = 0.318$ cm, $A_x = \pi(91.44 \times 17.15)$ cm²
49	Bottom array	38–39	10.74	$L = 0.953$ cm, $A_x = \pi(91.44 \times 35.56)$ cm²
50		39–40	3.582	$L = 0.318$ cm, $A_x = \pi(91.44 \times 35.56)$ cm² — Multilayer $k = 8.66 \times 10^{-6}$
54[a]		41–42	20.12	$L = 0.953$ cm, $A_x = \pi(91.44 \times 19.05)$ cm²
55[a]		42–43	6.689	$L = 0.318$ cm, $A_x = \pi(91.44 \times 19.05)$ cm²
44	Gas bottle	2–14	44.77	$L = 0.635$ cm, $A_x = 4\pi(11.43)^2$ cm² — Multilayer $k = 8.66 \times 10^{-6}$
45	Cylinder	12–13	89.53	$L = 1.27$ cm, $A_x = \pi(25.4 \times 20.32)$ cm² — Multilayer $k = 8.66 \times 10^{-6}$

See footnotes at end of table.

TABLE 23 (Cont.)

Resistor no.	Node description	Connecting nodes i-j	Resistance value °K/W	Assumptions
	Insulation resistance parallel to layers:			
7		16-22	547.8	$L = 17.78$ cm, $A_x = (1.27 \times \pi \times 45.72)$ cm^2, multilayer parallel to layers, $k = 0.173 \times 10^{-3}$
6	Top cover	16-23	547.8	
10		24-22	255.4	$L = 22.86$ cm, $A_x = (1.27 \times \pi \times 91.44)$ cm^2, multilayer parallel to layers, $k = 0.173 \times 10^{-3}$
9		24-23	255.4	
11	Upper array insulation	24-25	324.4	$L = 10.16$ cm, $A_x = (0.635 \times \pi \times 91.44)$ cm^2, multilayer parallel to layers, $k = 0.173 \times 10^{-3}$
12		24-26	324.4	
13	Upper array honeycomb substrate	24-27	13.85	$R = L_1/L_2$ (392), $L = 10.16$ cm, $W = (\pi \times 91.44)$ cm
16		25-32	59.36	$L = 18.73$ cm, $A_x = (0.635 \times \pi \times 91.44)$ cm^2, $k = 0.173 \times 10^{-3}$
17	Upper array to viewing band	26-33	593.6	
18		27-34	3160	Assumed high resistance because no direct connection.
21		32-10	273.9	$L = 8.573$ cm, $A_x = (0.635 \times \pi \times 91.44)$ cm^2, $k = 0.173 \times 10^{-3}$
22	Viewing band insulation to instrument platform	33-10	273.9	
23		34-10	3160	Assumed high resistance because no direct connection.
46	Instrument platform to lower insulation	11-38	566.7	$L = 17.78$ cm, $A_x = (0.635 \times \pi \times 91.44)$, $k = 0.173 \times 10^{-3}$
47		11-39	566.7	
48	Lower array honeycomb substrate	11-40	24.28	$R = L_1/L_2$ (392), $L = 17.78$ cm, $W = \pi(91.44)$ cm
51[a]	Lower insulation	38-41	866.9	$L = 27.31$ cm, $A_x = (0.635 \times \pi \times 91.44)$ cm^2, $k = 0.173 \times 10^{-3}$
52[a]		39-42	866.9	
53[a]	Lower array honeycomb substrate	40-43	37.29	$R = L_1/L_2$ (392), $L = 27.31$ cm, $W = \pi(31.44)$ cm
33[b]		16-15	2.634	Stainless steel tubing, $L = 17.78$ cm, $A_x = 0.79$ cm^2/tube, $k = 0.173$ Contact resistance assumed to be 4.74 Total resistance of one support = $R_1 = 1.32 \times 10^2$ Two supports are combined into one resistance by dividing R_1 by 2.
34[b]	Antenna base and motor to boom brackets	15-9	2.634	
55[b]		45-41	2.634	
56[b]		45-16	2.634	
37[b]		35-9	0.2634	Contact resistance assumed
36[b]	Boom brackets to experiment booms	36-35	6.900	Al tubing, $L = 76.2$ cm, 2.54 cm O.D., $A_x = 3.187$ cm^2, $k = 1.731$ Two booms combined.
35[b]		37-36	6.900	
53[b]		42-41	0.2634	Contact resistance assumed.
52[b]	Boom brackets to RTG booms	43-42	6.900	Al tubing, $L = 76.2$ cm, 2.54 cm O.D., $A_x = 3.187$ cm^2, $k = 1.731$ Two booms combined.
51[b]		44-43	6.900	
38[b]	Boom brackets to platform	9-10	27.39	Contact resistance assumed.
54[b]		41-10	27.39	

[a]Indicates resistance values peculiar to solar-powered configuration.

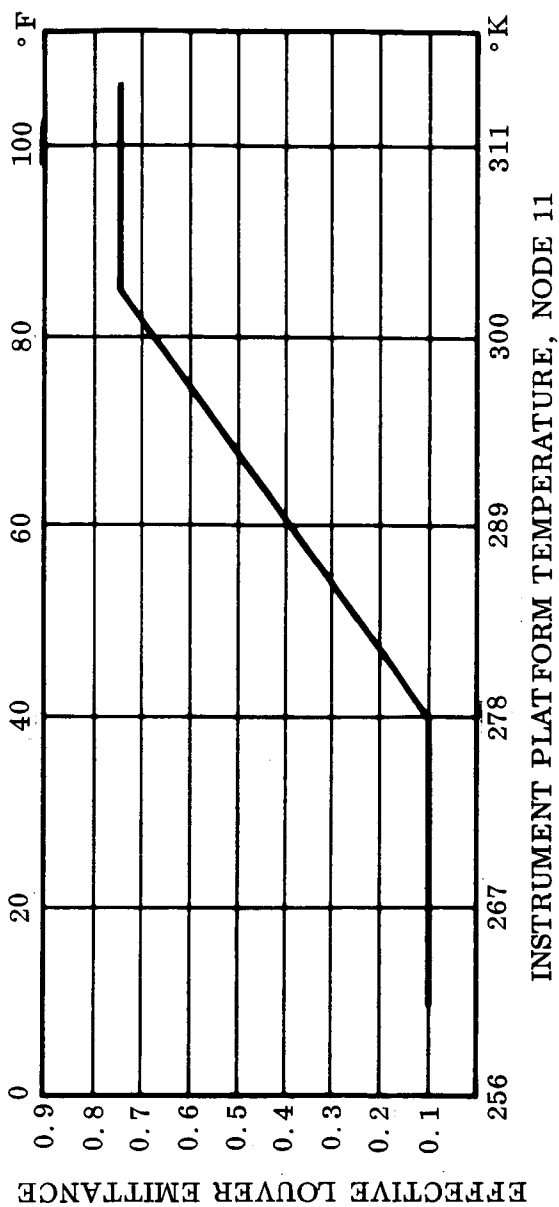[b]Indicates resistance values peculiar to RTG-powered configuration.

Figure 22   Effective Louver Emittance as a Function of Instrument Platform Temperature

TABLE 24. – THERMAL RADIATION EXCHANGE FACTORS

Resistor no.	Connecting nodes i	j	$RADK_{ij}$ $\frac{cm^2\text{-}hr}{sec}$	ϵ_i	ϵ_j	F_{ij}	A_i (cm^2)	Comments
101	21 (Antenna reflector)	1 (space)	2.759×10^{-1}	0.85	1.0	0.84	1387	White paint
102	21	1	2.926×10^{-1}	0.80		0.95	1387	OSR
103	20	1	2.025×10^{-1}	0.80		0.62	1387	White paint
104	20	1	2.313×10^{-1}	0.80		0.75	1387	OSR
105	19 (Antenna dipole)	1	1.356×10^{-1}	0.80		0.63	968	OSR
106	18	1	1.031×10^{-1}	0.80		0.48	968	OSR
107	17 (Antenna platform)	1	8.863×10^{-2}	0.05		0.79	1226	Polished Al
108	23 (Top cover)	1	8.268×10^{-2}	0.05		0.84	7097	Al side of multilayer insul.
109	24 (Top ring)	1	1.161×10^{-2}	0.05		1.00	839	Polished Al
110[a]	27 (Upper solar cell array)	1	1.384	0.82			6065	Solar cells
119[a]	40 (Lower solar cell array)	1	1.208	0.82			5323	Solar cells, 1/2 array shielded
124[a]	43	1	6.503×10^{-1}	0.82			2852	Solar cells, 1/2 array shielded
115	34 (Viewing band)	1	1.068	0.80			4820	OSR
111	28 (Sun sensors)	1	2.973×10^{-2}	0.80			133.88	White paint with holes
112	29 (Exps. No. 4 & 6)	1	1.607×10^{-2}	0.80			72.26	OSR with holes
113	30 (Exp. No. 7)	1	1.152×10^{-3}	1.00			4.168	Opening assumed to be blackbody
114	31 (Exp. No. 2)	1	2.536×10^{-3}	0.10			90.97	Al with holes
116[a]	35 (Booms)	1	9.179×10^{-2}	0.80		0.75	548.4	OSR – 1/4 of length
117[a]	36	1	2.434×10^{-1}	0.60		1.00	1097	OSR – 1/2 of length
118[a]	37	1	1.217×10^{-1}	0.80		1.00	548.4	OSR – 1/4 of length
120	38 (Lower array insulation)	1	2.072×10^{-2}	0.05		0.206	7226	Al side of multilayer insul.
123[a]	41	1	2.035×10^{-2}	0.05		0.266	5484	Al side of multilayer insul.
122	12 (Cylinder outside)	1	1.700×10^{-3}	0.05		0.083	1465	Al side of multilayer insul.
126	13 (Cylinder inside)	1	4.877×10^{-3}	0.17		$F_{ij}A_i = 103.2$		Mg cylinder, bottom removed
127	14 (Sphere)	1	2.694×10^{-3}	0.05		$F_{ij}A_i = 193.6$		Al side of multilayer insul.
121	11 (Louvers)	1	1.226×10^{-1} to 9.197×10^{-1}	0.10 to 0.75		0.340	4452	$RADK_{ij}$ and ϵ_i are linear functions of node 11 temp. from 277°K (closed) to 302°K (open)
123[b]	42 (RTG)	1	6.039×10^{-2}	0.80		0.75	361	OSR
124[b]	43 (Booms)	1	1.616×10^{-1}			1.00	729	
125[b]	44 (Booms)	1	2.295			1.00	10323	
116[b]	35 (Experiment)	1	6.039×10^{-2}			0.75	361	
117[b]	36 (Booms)	1	1.616×10^{-1}			1.00	729	
118[b]	37 (Booms)	1	8.008×10^{-2}				361	
110[b]	27 (Upper array)	1	1.347				6065	
119[b]	40 (Lower array)	1	2.369				10646	OSR
201	18 (Dipole)	17 (Ant. platform)	1.607×10^{-3}		0.05	0.15	968	
202		20 (Reflector)	3.289×10^{-2}		0.85	0.18	968	

See footnotes at end of table.

TABLE 24 (Cont.)

Resistor no.	Connecting nodes i	Connecting nodes j	$RADK_{ij}$ $\frac{cm^2-hr}{sec}$	ϵ_i	ϵ_j	F_{ij}	A_i (cm^2)	Comments
203	18 (Dipole)	21 (Reflector)	7.302×10^{-3}	0.80	0.85	0.04	968	
204		23 (Top cover outside)	1.607×10^{-3}		0.05	0.15		
205	19 (Dipole)	17 (Antenna platform)	4.292×10^{-4}		0.05	0.04		
206		20 (Reflector)	2.369×10^{-2}		0.85	0.13		
207		21 (Reflector)	2.750×10^{-2}		0.85	0.15		
208		23 (Top cover outside)	4.292×10^{-4}		0.05	0.04		
209	23 (Top cover outside)	20 (Reflector)	3.670×10^{-3}	0.05	0.85	0.10	3110	Front of reflector
210		20 (Reflector)	4.013×10^{3}		0.80	0.14	2581	Back of reflector
211		21 (Reflector)	3.670×10^{-4}		0.85	0.01	3110	Front of reflector
212		21 (Reflector)	8.565×10^{-4}		0.80	0.03	2581	Back of reflector
213	17 (Platform)	20 (Reflector)	1.904×10^{-3}		0.85	0.13	1239	Front of reflector
214		21 (Reflector)	2.880×10^{-4}		0.85	0.02	1239	Front of reflector
215		23 (Top cover outside)	8.593×10^{-4}		0.05	1.00	1239	
216	16 (Motor & base)	25 (Upper array insulation)	2.880×10^{-4}	0.10	0.05	0.17	123	Base is 12.7 cm dia.
217		32 (Viewing band insulation)	1.356×10^{-4}		0.05	0.08		
218		3 (DTU)	8.547×10^{-5}		0.10	0.25		$A_3 = 387 \text{ cm}^2$
219		4 (Other equipment)	5.110×10^{-5}		0.10	0.15		$A_4 = A_{10} =$ $\frac{\pi(45.72^2-12.7^2)-516}{2} \text{ cm}^2$
220		5 (Exp. No. 2)	1.672×10^{-5}			0.05		$A_5 = 155 \text{ cm}^2$
221		6 (Exp. No. 7)	1.672×10^{-5}			0.05		$A_6 = 232 \text{ cm}^2$
222		7 (Exps. No. 4 & 6)	3.437×10^{-5}			0.10		$A_7 = 516 \text{ cm}^2$
223		10 (Exp. platform)	5.110×10^{-5}			0.15		$A_4 = A_{10} = 2774 \text{ cm}^2$
224	22 (Top cover inside)	25 (Upper array insulation)	1.431×10^{-3}	0.05	0.05	0.32	5839	
225	22 (Top cover inside)	32 (Viewing band insulation)	3.577×10^{-4}		0.05	0.08		
226		3 (DTU)	8.956×10^{-4}		0.10	0.10		
227		4 (Other equipment)	1.347×10^{-3}			0.15		
228		5 (Exp. No. 2)	4.478×10^{-4}			0.05		
229		6 (Exp. No. 7)	4.478×10^{-4}			0.05		
230		7 (Exps. No. 4 & 6)	8.956×10^{-4}			0.10		
231		10 (Exp. platform)	1.347×10^{-3}			0.15		
232	25 (Upper array insulation)	10 (Exp. platform)	3.140×10^{-3}			0.30	6839	
233	32 (Viewing band insulation)	10 (Exp. platform)	2.926×10^{-3}			0.40	4774	
234	3 (DTU)	14 (Sphere)	2.694×10^{-4}	0.10	0.05	0.50	387	
235	14 (Sphere)	13 (Cylinder)	2.555×10^{-4}	0.05	0.17	0.70	1548	
238	12 (Cylinder outside)	38 (Lower array insulation)	4.069×10^{-3}	0.05	0.05	0.40	1465	

See footnotes at end of table.

77

TABLE 24 (Cont.)

Resistor no.	Connecting nodes		$RADK_{ij}$ $\frac{cm^2-hr}{sec}$	Radiative characteristics				Comments
	i	j		ϵ_i	ϵ_j	F_{ij}	A_i (cm^2)	
240	12 (Cylinder outside)	41 (Lower array insulation)	1.886×10^{-4}	0.05	0.05	0.17	1594	
236	11 (Louvers)	12 (Cyl. outside)	6.187×10^{-4} to 4.645×10^{-3}	0.10 to 0.75		0.10	4452	$RADK_{ij}$ and ϵ_i are linear functions of node 11 temp. from 277°K (closed) to 302°K (open)
237	11 (Louvers)	38 (Lower array insulation)	2.480×10^{-3} to 1.858×10^{-2}			0.40		
239[a]	11 (Louvers)	41 (Lower array insulation)	9.290×10^{-4} to 6.968×10^{-3}			0.15		
239[b]	44 (RTG's)	21 (Reflector)	8.826×10^{-3}	0.80	0.80	$F_{ij}A_i = 49.7$		$F_{ij}A_i$ products were obtained by summing data of NASA Hr 4 BD of 2-4-66
240[b]		20 (Reflector)	8.826×10^{-3}			$F_{ij}A_i = 49.7$		
241[b]		19 (Dipole)	1.486×10^{-3}			$F_{ij}A_i = 8.39$		
242[b]		18 (Dipole)	1.486×10^{-3}			$F_{ij}A_i = 8.39$		
243[b]		27 (Upper array)	3.995×10^{-3}			$F_{ij}A_i = 22.6$		
244[b]		34 (Viewing band)	4.812×10^{-3}			$F_{ij}A_i = 27.1$		
245[b]		40 (Lower array)	8.826×10^{-3}			$F_{ij}A_i = 49.7$		

[a]Indicates $RADK_{ij}$ values peculiar to solar-powered configuration.

[b]Indicates $RADK_{ij}$ values peculiar to RTG-powered configuration.

Node	Temp. (°K) at 1.0 AU	Temp. (°K) at 0.2 AU
1 (outer space)	0	0
2	234	240
3	284	293
4	287	295
5	285	293
6	284	294
7	284	294
8	2	294
9	194	332
10	284	293
11	284	292
12	270	280
13	284	291
14	230	234
15	204	400
16	213	468
17	228	455
18	213	481
19	208	463
20	238	543
21	233	519
22	200	348
23	180	320
24	262	468
25	274	497
26	280	598
27	284	636
28	284	294
29	284	294
30	285	294
31	285	293
32	162	310
33	150	307
34	144	304
35	193	332
36	182	333
37	182	380
38	285	303
39	314	346
40	324	360
41	274	287
42	321	342
43	336	360

Figure 23 Temperature Distribution for Solar-Powered Configuration at 1.0 and 0.2 AU

79

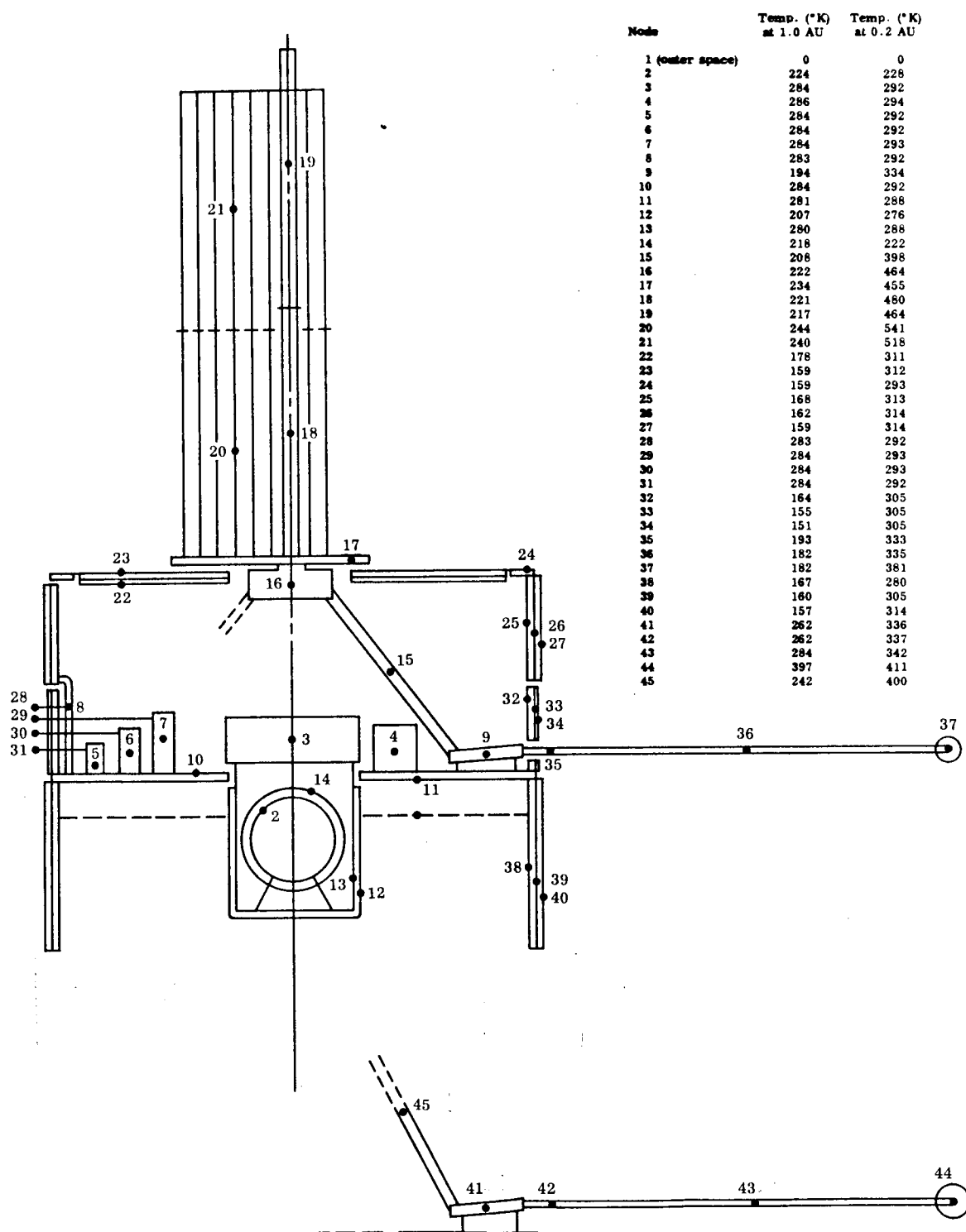| Node	Temp. (°K) at 1.0 AU	Temp. (°K) at 0.2 AU
1 (outer space)	0	0
2	224	228
3	284	292
4	286	294
5	284	292
6	284	292
7	284	293
8	283	292
9	194	334
10	284	292
11	281	288
12	207	276
13	280	288
14	218	222
15	208	398
16	222	464
17	234	455
18	221	460
19	217	464
20	244	541
21	240	518
22	178	311
23	159	312
24	159	293
25	168	313
26	162	314
27	159	314
28	283	292
29	284	293
30	284	293
31	284	292
32	164	305
33	155	305
34	151	305
35	193	333
36	182	335
37	182	381
38	167	280
39	160	305
40	157	314
41	262	336
42	262	337
43	284	342
44	397	411
45	242	400

Figure 24 Temperature Distribution for RTG-Powered Configuration
at 1.0 and 0.2 AU